



THE UNIVERSITY *of* EDINBURGH

Edinburgh Research Explorer

The effect of melt composition and oxygen fugacity on manganese partitioning between apatite and silicate melt

Citation for published version:

EIMF, Stokes, TN, Bromiley, GD, Potts, NJ, Saunders, KE & Miles, AJ 2019, 'The effect of melt composition and oxygen fugacity on manganese partitioning between apatite and silicate melt', *Chemical Geology*, vol. 506, pp. 162-174. <https://doi.org/10.1016/j.chemgeo.2018.12.015>

Digital Object Identifier (DOI):

[10.1016/j.chemgeo.2018.12.015](https://doi.org/10.1016/j.chemgeo.2018.12.015)

Link:

[Link to publication record in Edinburgh Research Explorer](#)

Document Version:

Peer reviewed version

Published In:

Chemical Geology

General rights

Copyright for the publications made accessible via the Edinburgh Research Explorer is retained by the author(s) and / or other copyright owners and it is a condition of accessing these publications that users recognise and abide by the legal requirements associated with these rights.

Take down policy

The University of Edinburgh has made every reasonable effort to ensure that Edinburgh Research Explorer content complies with UK legislation. If you believe that the public display of this file breaches copyright please contact openaccess@ed.ac.uk providing details, and we will remove access to the work immediately and investigate your claim.



1 Declarations of interest: none

2

3 **The effect of melt composition and oxygen fugacity on manganese partitioning between apatite**
4 **and silicate melt**

5 T.N. Stokes^{1*}, G. D. Bromiley¹, N. J. Potts¹, K. E. Saunders¹, A. J. Miles², EIMF¹

6 ¹School of GeoSciences, Grant Institute, Kings Buildings, University of Edinburgh, Edinburgh, UK.

7 ²School of Geography, Geology and the Environment, University of Leicester, University Road,
8 Leicester LE1 7RH, UK

9

10 *Corresponding Author: thomas.stokes@ed.ac.uk

11 **Abstract:**

12 Oxygen fugacity and melt composition are both known to have a strong influence on the partitioning
13 of trace elements between coexisting minerals and melt. Previous work has suggested that Mn
14 partitioning between apatite and silicate melt may be strongly affected by oxygen fugacity and could,
15 therefore, act as an oxybarometer. Here, we present a new study on the partitioning of Mn between
16 apatite and melt at high temperature (1400-1250 °C) and 1 GPa pressure, for various melt
17 compositions and oxygen fugacities (NNO +4.7 to NNO -10). We find that there is no demonstrable
18 variation in the partition coefficient for Mn between apatite and silicate melt (D_{Mn}^{Ap-m}) across the
19 range of fO_2 conditions studied here. Instead, we find that D_{Mn}^{Ap-m} varies significantly with melt
20 composition and that in particular, the proportion of non-bridging oxygens strongly influences
21 partitioning of Mn between apatite and melt. We propose that variations in the Mn content of natural
22 apatite, previously thought to reflect variations in fO_2 , are instead related to the degree of melt
23 polymerization. These findings are consistent with the results of Mn K-edge XANES spectroscopy,
24 which demonstrate that Mn in coexisting apatite and silicate glass is present predominantly as Mn^{2+}
25 regardless of fO_2 . Furthermore, XANES spectra from a series of silicate glasses synthesised at various
26 oxygen fugacities demonstrate that Mn^{2+} is the predominant species, and that the average Mn
27 oxidation state does not vary over a wide range of fO_2 -T conditions.

28 **Keywords:** Apatite, Manganese, element partitioning, oxygen fugacity, experimental petrology, melt
29 composition

30 **Introduction:**

31 Apatite [nominally $\text{Ca}_5(\text{PO}_4)_3(\text{F,Cl,OH})$] is an accessory mineral found in many igneous, metamorphic,
32 and sedimentary rocks. The three primary apatite end-members (fluor-, chlor- and hydroxyapatite)
33 relate to the three anion end members of apatite (F, Cl and OH respectively). The incorporation of
34 these volatiles as major constituents in the apatite crystal structure make it a critical mineral for
35 understanding melt volatile contents in terrestrial (Douce and Roden 2006; Scott et al. 2015) and
36 extra-terrestrial systems (Gross et al. 2013; McCubbin et al. 2016). Apatite is also an important tool
37 for exploring the trace element budgets of magmas (Nagasawa 1970; Sha and Chappell 1999), as its
38 crystallographic structure allows for the incorporation of more than half the stable naturally-occurring
39 elements (Hughes 2015). Recent work (Miles et al. 2014; Konecke et al. 2017) has also suggested that
40 the substitution of redox sensitive elements (e.g. Mn, S, Ce, Eu) into apatite could be used to constrain
41 the oxygen fugacity ($f\text{O}_2$) of the melt from which it has crystallized, providing a much needed new
42 oxybarometer.

43 Oxygen fugacity is an important parameter within igneous systems because, among other things, it
44 controls mineral stabilities (Hensen 1986; Toplis and Carroll 1995), dictates gas species released from
45 volcanoes (Wallace and Carmichael 1992; Moussallam et al. 2016), and has implications on the
46 metallogenesis of primary igneous ore bodies (Fleet et al. 1991). Furthermore, estimates of $f\text{O}_2$ are
47 used in modelling geophysical processes in the mantle (e.g. creep, electrical conductivity; Ryerson et
48 al. 1989; Wood and Nell 1991; Dai and Karato 2014) and understanding the timing of planetary scale
49 processes, such as the oxidation of the mantle and atmosphere (Scaillet and Gaillard 2011). Oxygen
50 fugacity is also an important variable when constraining the composition of the earth's core (Li and
51 Agee 2001) and early continental crust (Yang et al. 2014), as well as for the timing of the onset of plate
52 tectonics (Brounce et al. 2015). However, despite the importance of $f\text{O}_2$ it remains one of the most

53 difficult geological parameters to accurately constrain. As such, any dependence of chemical
54 substitutions in apatite on fO_2 would be invaluable in constraining planetary processes.

55 Manganese in apatite is a minor element that can substitute for more than 1 atom per formula unit
56 (a.p.f.u.) onto the Ca₂ and P sites (Hughes et al. 2004; Deer et al. 2013). Several studies have indicated
57 that while partitioning of Mn between apatite and silicate melt is sensitive to oxygen fugacity, it is also
58 dependent on parameters such as melt SiO₂ and total alkali content, as well as melt structure (Sha and
59 Chappell 1999; Belousova et al. 2001; Chu et al. 2009; Miles et al. 2014). This work aims to constrain
60 the sensitivity of Mn partitioning between apatite and melt to fO_2 for a variety of silicate melt
61 compositions and to assess its viability as an oxybarometer.

62 1.1 Experimental rationale

63
64 We primarily set out to test the conclusion of Miles et al. (2014) that the Mn content of apatite, from
65 a range of calc-alkaline intermediate to silicic rocks, can be directly related to fO_2 via the below
66 empirical relationship:

$$67 \log fO_2 = -0.0022 (\pm 0.0003) Mn (ppm) - 9.75 (\pm 0.46) \quad [1]$$

68 This dependence implies that variations in fO_2 influence Mn apatite-melt partitioning because of a
69 change in the relative proportions of Mn oxidation states in the melt (Mn can be found in the 2+, 3+,
70 4+, and 5+ oxidation states in nature). However, under most geological conditions, Mn²⁺ is by far the
71 dominant species in silicate melts (Watson 1977, Schmidt et al. 2006). In apatite, Mn²⁺ has an ionic
72 radius of 0.90 Å in 7-fold (Shannon 1976) and 1.0 Å in 9-fold coordination (Miles et al. 2014). The
73 corresponding values for Ca²⁺ are 1.06 Å and 1.18 Å (Shannon 1976). Mn³⁺ has a smaller ionic radius
74 (0.62-0.67 Å; Miles et al. 2014); hence Mn²⁺ should preferentially partition into apatite from the melt
75 compared to Mn³⁺. However, Marks et al (2016) questioned the general applicability of a Mn-in-
76 apatite oxybarometer, suggesting that additional controls such as temperature, melt composition and
77 the co-precipitation of other Mn-bearing phases may also influence the Mn content of natural apatites.

78 We have conducted an experimental calibration of Mn oxidation state in silicate melts as a function
79 of fO_2 , in order to investigate its impact on apatite-melt partitioning. Experiments were designed to
80 examine how Mn oxidation state, in both apatite and melt, vary as a function of fO_2 for a range of melt
81 compositions. Apatite in three end-member melt compositions, ranging from basaltic andesite to
82 rhyolitic, were chosen so that any effects of crystal chemistry and melt composition on Mn partitioning
83 could also be determined.

84 *1.2 Starting Materials*

85 Starting materials consisted of mixtures of high-purity analytical oxide (SiO_2 , Al_2O_3 , TiO_2 , MgO , Fe_2O_3 ,
86 MnO_2) and carbonate ($CaCO_3$, Na_2CO_3 , and K_2CO_3) powders. Before use, powders were fired using the
87 following conditions: SiO_2 8 hours 1250 °C, TiO_2 16 hours 1000 °C, Al_2O_3 18 hours 1250 °C, Fe_2O_3 1 hour
88 800 °C, MgO 18 hours 1250 °C, $CaCO_3$ 4 hours 400 °C, Na_2CO_3 12 hours 400 °C and K_2CO_3 8 hours 500°C.
89 Following firing, powders were stored in a 110 °C oven. The starting compositions were ground under
90 acetone, using an agate mortar and pestle, for thirty minutes, to ensure homogeneity. Powders were
91 then loaded in a box furnace and decarbonated using a controlled heating program, which ramped
92 the temperature from 600- to 1000 °C over a 6 hour period. Following decarbonation, an apatite
93 component consisting of various amounts of tri-calcium phosphate [TCP- $Ca_3(PO_4)_2$] and either CaF_2 or
94 $CaCl_2$ was added to the starting material, and the mixture was reground for a further thirty minutes in
95 acetone. At this stage, water (1.5 wt. % H_2O) was also added to the SH3 and BMT2 starting
96 compositions in the form of gibbsite ($Al(OH)_3$) or brucite ($Mg(OH)_2$). The different bulk starting
97 compositions used in this study can be found in Table 1. Note PM1 and HAP10 were two iterations of
98 the same starting compositions.

99 *1.3 Experimental Procedures*

100 Experiments were carried out in an end-loaded piston cylinder, using ½" talc-pyrex assemblies with an
101 internal graphite resistance furnace, and inner crushable alumina spacers. Runs were first pressurised
102 to ~0.3 GPa before heating, then pressurised simultaneously with temperature, which was raised at a

103 rate of 100 °C/min. After reaching super liquidus conditions runs were slightly over pressurised to
104 compensate for pressure loss during the first hour (hot piston out technique). Temperature was
105 continuously monitored using a Pt₁₀₀–Pt₈₇Rh₁₃ thermocouple placed ≈10 °C from the hot spot of the
106 assembly. All experiments were run at 1 GPa.

107 Runs were initially taken to super liquidus conditions (Table 2) to ensure the homogeneity of the
108 starting composition and promote growth of larger apatite crystals. Subsequently, the temperature
109 was cooled isobarically to the final T at different rates (see Table 2). The final T and dwell time for each
110 run (Table 2) was chosen to ensure apatite was the only phase present within the melt, allow
111 equilibration between crystals and melt, and to also ensure apatite grains and areas of glass were a
112 suitable size for analysis. On completion of the run samples were isobarically quenched by shutting
113 off power to the heating circuit; T dropped to <50 °C in less than 30 seconds.

114 Oxygen fugacity was variably controlled in experiments by the sample environment. Initial runs were
115 carried out using a single Pt capsule, which is assumed to have an oxygen fugacity in the vicinity of the
116 Ni – NiO (NNO) solid buffer. Although fO_2 cannot be determined directly from the run products, it can
117 be estimated by comparison with other experiments run using the same experimental procedure. In
118 a separate series of experiments, run using the same bulk composition but doped with Eu, with the
119 same sample preparation procedure and sample assembly, Eu XANES spectra indicate an Eu^{2+}/Eu^{3+}
120 ratio in the melt phase close to that of the NNO buffer, as expected (Burnham et al. 2015).

121 A second suite of experiments were carried out using an inner graphite bucket inside a Pt capsule. As
122 described by Médard et al. (2008), the presence of a graphite liner in the Pt capsule results in buffering
123 of O by reaction with C, and more reducing conditions close to C - CO (CCO-1; Médard et al. 2008).
124 Again, we cannot verify fO_2 conditions directly in these experiments, and it is possible that use of a Fe-
125 free starting material here, for example, could result in slightly more reduced conditions than those
126 described by Médard et al. (2008). However, it is unlikely that fO_2 conditions in graphite-Pt capsules
127 will be more oxidising than CCO (Médard et al. 2008), providing a more reducing conditions than

128 samples run in just Pt or with an oxidising buffer. Oxygen fugacity in subsequent experiments was
129 controlled using a double capsule technique (e.g., Eugster 1957; Eugster and Wones 1962; Jakobsson
130 2012). In these runs, f_{O_2} was controlled using a series of metal-metal oxide oxygen buffers (i.e. Ni-
131 NiO, Cr-Cr₂O₃, Fe₃O₄-Fe₂O₃, Fe₃O₄-FeO) within an outer Pt capsule that enveloped an internal Pt
132 capsule containing the starting material. Four μ L of deionized (DI) water was micro-syringed into the
133 bottom of all outer capsules regardless of starting composition prior to filing with the buffer and
134 welding. In the CaCl₂ starting composition runs, 4 μ L of DI water was added into the inner capsule prior
135 to filing and welding. Calculated oxygen fugacity values are given in Table 2 and were calculated based
136 on the relevant redox buffer equations (Holzheid and O'Neill 1995, Jakobsson 1985, Médard et al.
137 2008, O'Neill 1988, O'Neill and Pownceby 1993). The f_{O_2} values for experiments run with a solid state
138 buffer could deviate from the calculated buffer values if the activity of water inside the capsule is not
139 in unity, and in water under-saturated samples, f_{O_2} values will be lower than the coexisting hydrated
140 buffer (Matjuskin et al. 2015), and indicated in Table 2. The purpose of high-pressure experiments
141 here, however, due to complexities in experimental design, is to synthesise apatite in equilibrium with
142 silicate melt under a range of f_{O_2} conditions, from oxidising to reducing. Gas-mixing synthesis
143 experiments are then used to accurately constrain the influence of f_{O_2} on Mn oxidation state.

144 Additional experiments were carried out in a vertical tube gas mixing furnace to synthesise Mn bearing
145 glasses at controlled f_{O_2} conditions, at atmospheric pressure. A Mn-Fe doped granitic starting
146 composition and a Mn doped granitic starting composition was mixed with poly-vinyl acetate (PVA) to
147 create beads, each bead was hung on the end of a Pt loop. Multiple beads were organised on a
148 chandelier and placed in the hot-spot of the furnace on the end of an alumina rod. Redox conditions
149 inside the furnace were determined using CO₂-H₂ mixtures, with in line Bronkhorst mass flow
150 controllers to regulate gas proportions as calculated using the tables of Deines (1970). All experiments
151 were held at 1300 °C for 24 hours to equilibrate before being rapidly quenched by quickly raising the
152 alumina rod out of the hot-spot.

153 **1.4 Analytical Techniques: EPMA**

154 Recovered capsules were mounted in crystal bond, ground to the desired level, and polished using
155 diamond paste. Crystal bond was later dissolved using acetone. After cleaning, samples were mounted
156 in 1" indium mounts and carbon coated. Glass beads from the gas mixing furnace experiments were
157 embedded in epoxy, ground, and polished prior to analysis. Electron probe microanalysis data was
158 collected using the JEOL JXA8530F Hyperprobe field emission gun electron microprobe analyser (FEG-
159 EPMA) at the University of Bristol.

160 Apatite was analysed using a 10 µm beam for all conditions; the first protocol measured Na, Ca, P, F,
161 and Cl with an accelerating voltage of 15keV and 5nA current. The second protocol used a 15 keV
162 accelerating voltage and 20nA current to measure Si, Mg, K, S, Fe, Mn, Ni, Cr, and Ti on the same spot
163 as the first protocol. Standards used were albite (Na, Si), Saint John's Island olivine (Mg), sanidine (K),
164 barite (S), NaCl (Cl), fayalite (Fe), Mn metal (Mn), Ni metal (Ni), Cr₂O₃ (Cr), TiO₂ (Ti), and Durango
165 apatite (Ca, P, F).

166 The glass was analysed with the following conditions: (1) 15keV accelerating voltage, 10nA current for
167 Ca, Ti, Si, Al, Na, Mg, F, K, Cl, Fe and Ni (2) 15keV accelerating voltage, 40nA current for Mn, Cr, and P.
168 All analyses were collected with a 10 µm beam and both protocols analysed the same spot. Standards
169 were as follows: wollastonite (Ca), Saint John's Island olivine (Mg), TiO₂ (Ti), albite (Si, Na), MgF₂ (F),
170 sanidine (Al, K), NaCl (Cl), fayalite (Fe, Mn), Cr₂O₃ (Cr), Durango apatite (P), and Ni metal (Ni).

171 **1.5 Analytical Techniques: SIMS**

172
173 Volatile measurements in the apatite and coexisting glasses were collected by secondary ion mass
174 spectrometry (SIMS) on a Cameca ims-4f at the NERC ion probe facility at the University of Edinburgh.
175 Prior to SIMS analysis samples were cleaned with ethanol, and then coated with ~35 nm gold to
176 provide electrical conductivity.

177 Analyses were done using a 16O^- primary beam with nominal current of 2.2nA, and 10.8KeV
178 accelerating voltage was targeted on a sample with a 4.5keV voltage to produce a $\sim 15\text{keV}$ net impact
179 energy. Apatite and glass measurements of the secondary ions 1H , 11B , 12C , 16O , 19F , 26Mg , 30Si ,
180 31P , 35Cl , 39K , 42Ca , 55Mn , 88Sr , 138Ba , 139La , 140Ce and 151Eu were counted on an electron
181 multiplier for 79 seconds respectively, for each 6 cycles of the magnet. A 3-minute pre-sputter period
182 at a raster size of $10\mu\text{m}$ was used to pre-clean the analysis area. Secondary ions were acquired with a
183 $25\mu\text{m}$ diameter image field, and the area analysed was restricted to $8\text{-}10\mu\text{m}$ spot size using a circular
184 field aperture. An energy offset of 50eV was applied (40eV window). Higher resolution CO_2
185 measurements of glass and apatite were collected on additional spots (size permitting). These were
186 acquired after a 4-minute pre sputter, with a $20\mu\text{m}$ raster, to pre clean the analysis area. Data was
187 collected with a $60\mu\text{m}$ diameter image field, 50eV offset (40eV window), and a field aperture was used
188 to restrict ions to a spot size of $\sim 15\mu\text{m}$ in diameter. The mass resolution employed was 900-1000,
189 which is sufficient to separate 25Mg^{2+} from 12C^+ . The majority of CO_2 measurements reported for
190 apatite are based on the low-resolution window measurements, using higher resolution measurement
191 to identify the need of an Mg correction. An Mg^{2+} correction based on 25Mg^{2+} was applied.

192 Only SIMS measurements for H_2O and CO_2 are given here, quantified by the 1H and 12C isotopes
193 respectively. Other elements were measured to confirm that the analyses were not contaminated,
194 and Eu/Ce measurements are for use in future investigation. Apatite standards (Bristol in-house
195 standards – Riker et. al 2018) were used to quantify ion yields for 1H , and CO_2 analyses based on H/Ca
196 and C/Ca ratios. Basaltic glass standards (ST-2 and ST-6) were used to quantify ion yields for 1H , and
197 CO_2 analyses based on H/Si and C/Si . Absolute error for SIMS data is assumed to be better than 10%.

198 *1.6 Analytical Techniques: XANES*

199

200 Mn and Fe K-edge XANES spectra were collected on experimental capsules and glasses in 1" epoxy
201 mounts at beamline I18 of the Diamond Light Source (Harwell, UK) in one three-day session. These
202 samples were then removed from epoxy for subsequent analysis techniques (EPMA, SIMS). Spectra

203 were acquired in fluorescence mode, using a Ge detector. Beam energy was finely tuned using a Si(111)
204 crystal monochromator. The beam size was selected by using a variety of slits and was focussed on an
205 area of $5\ \mu\text{m} \times 5\ \mu\text{m}$. Mn K-edge scans were measured over an energy range of 6400-6750 eV with a
206 1s count time per point. The pre-edge region was measured in 5 eV steps from 6400-6520 eV and from
207 6520-6532 eV with 1 eV steps. The edge region from 6532-6562 eV was measured with 0.2 eV steps
208 and 6562-6580 eV with 1 eV steps. The post-edge region was collected with 3 eV steps from 6600-
209 6750 eV. Mn K-edge energy was calibrated by defining the first inflection point in the derivative of a
210 Mn foil standard to 6539 eV.

211 Fe K-edge spectra were collected from 7000-7320 eV with a 1s count time per point. The pre-edge
212 region was measured from 7000-7090 eV with 6.25 eV steps, and from 7090-7107 with 1 eV steps.
213 The edge region was scanned with 0.25 eV steps from 7107-7120, 0.3eV steps from 7120-7140 eV and
214 1 eV steps over 7140-7160 eV. The post edge region from 7160-7320 was measured with 3 eV steps.
215 Fe spectra energy was calibrated to the first inflection point in the derivative of a Fe foil standard to
216 7112 eV.

217 Multiple Fe and Mn XANES scans on a same sample were taken to check for a change in oxidation with
218 beam exposure. Additional repeat scans were taken on the same sample but at additional spots at the
219 start and end of the beamline session to check the reproducibility of the runs. No obvious shift in the
220 pre-edge energy position was noted for spectra collected at the start and end of the session which is
221 in fitting with the findings of Mosselmans et al. (2009), that the pre-edge position of Ti for scans taken
222 36 hours apart on beamline I18 shifted by $\sim 0.03\text{eV}$, which is less than the resolution of the beamline.

223 Raw data was imported into the software Athena (Ravel and Newville 2005), where multiple scan data
224 was merged. Scans were also deglitched, corrected for self-absorption based on the FLUO algorithm
225 (Haskel 1999) and then the data was pre-edge/post-edge normalised.

226 Pre-edge peak fitting was carried out on the normalised data in Fityk (Wojdyr 2010). Pre-edge peaks
227 were obtained from the data by fitting a convex hull spline baseline across the pre-edge region.

228 Gaussian peaks of fixed half-width at half-maximum of 0.7 were fitted to the data. All data was fit
229 assuming two Gaussian contributions. The Gaussian contributions were used to calculate the average
230 integrated intensity for each fit, and was calculated from the sum of the integrated intensities of each
231 contributing peak. The 'average' centroid position was calculated from the area weighted centroid
232 positions of each Gaussian peak.

233 **Experimental Results**

234 All run products contained apatite and quenched melt (glass). In run PM1 H an additional unidentified
235 mineral phase was found. Apatite throughout the experiments varies in size from 2 to 500 μ m, in the
236 longest dimension, with the largest apatite found in the least silicic melts. Modal proportions of
237 apatite crystals are generally less than 30% and the habits of most crystals are euhedral. Apatite
238 commonly display elongate melt inclusions trapped in their cores, running parallel to the longest axis
239 of the crystals. Major, trace, and volatile measurements for glasses from each group of starting
240 compositions are listed in Table 2. Quenched glasses for all runs are homogenous in appearance and
241 have low standard deviation in major and minor element analyses. Apatites reveal no evidence of
242 chemical zonation. Furthermore, standard deviations for major and minor elements, calculated for
243 multiple analyses, are low (Table 3), and comparable to errors on individual analyses calculated by
244 JEOL software from counting statistics. This suggests that all our experiments are in equilibrium.

245 Glass compositions for runs with the PM1/Hap10 starting mix resulted in a range of compositions from
246 trachyte to phonotephroite/basaltic trachyandesite (Fig. 1). This range is due to varying degrees of
247 apatite saturation, and the additional effect of crystallising another phase in PM1 H. This also resulted
248 in different degrees of melt polymerisation as quantified by the ratio of non-bridging oxygens to
249 tetrahedrally coordinated cations (NBO/T). PM1 H contained the most polymerised melt upon
250 quenching (NBO/T = 0.12) and PM1 Pt the least (NBO/T = 0.43; Table 2), while the average NBO/T for
251 the PM1/Hap10 quenched glasses \approx 0.26. MnO contents of the glasses vary from a minimum of 4.31
252 wt% in PM1 H to 9.21 wt% in PM1 Pt. Apatite from the PM1/Hap10 experiments has a range of Mn

253 contents from 4.94 wt% MnO (0.74 a.p.f.u. PM1 Pt) to 7.89 wt% MnO (1.16 a.p.f.u. - PM1 NNO), with
254 an average of 6.51 wt% MnO. Molar proportion of Cl-H₂O for these apatite displays a range from more
255 Cl rich ($X^{\text{Ap}}_{\text{Cl}} = 0.89$, PM1 Pt) in the PM1 samples to closer to pure hydroxyapatite compositions ($X^{\text{Ap}}_{\text{H}_2\text{O}}$
256 = 0.90, Cr 1200 Hap10) in HAP10 runs.

257 Sample Cr 1200 Hap5 was run in an additional starting composition (Table 1). Hap 5 is similar in
258 composition to Hap10 but contained half the amount of Mn (5 wt.%). This experiment resulted in a
259 trachytic glass composition. Apatite in this run contained 6.58 wt% MnO (0.96 a.p.f.u.) and the anion
260 content is close in composition to the hydroxyl end member ($X^{\text{Ap}}_{\text{H}_2\text{O}} = 0.85$).

261 The SH3 composition resulted in glasses that are basaltic in composition, ranging from 4.00-4.32 wt%
262 total alkalis (Na₂O + K₂O) and 45.42-46.47 wt% SiO₂ (Fig. 1). SH3 MH shows elevated FeO levels (1.75
263 wt% FeO) compared to other samples in this composition, presumably due to contamination from the
264 buffer, occurring because of diffusion of Fe through the Pt into the sample. The MnO contents in these
265 samples ranges from a minimum of 0.73 wt% MnO in SH3 Cr to a maximum of 0.90 wt% MnO in SH3
266 Pt. Apatite from this composition contains 0.90 wt% MgO (0.22 a.p.f.u.), and a maximum of 0.19 wt%
267 MnO (0.03 a.p.f.u.). All apatite are close to the F end member composition with X^{Ap}_{F} ranging from
268 0.86-0.96 (Table 3).

269 Experiments run in the BMT2 system, with the exception of BMT2 MH, contain glasses that range from
270 tephriphonolite to phonolite in composition (Fig. 1). Sample BMT2 MH was subject to Fe
271 contamination from the buffer, with the addition of 12.1wt% FeO^T that changed the glass composition
272 to a Fe-rich foidite (Fig. 1). The MnO content varied between 0.07-0.80 wt% in these quenched glasses,
273 thought to be a result of differences in the amount of apatite crystallised. Apatite from this starting
274 composition contained variable amounts of Mn compared to SH3, with 0.02, 0.04 and 0.07 a.p.f.u. of
275 Mn for samples BMT2 Cr, MH and Pt respectively. BMT2 Cr is closest in composition to end member
276 FAp (3.53 wt. %), whilst BMT2 Pt has the least amount of F (3.26 wt. %).

277 The compositions of 1 atm. gas mixing furnace glasses are given in Table 4. Both set of glasses are
278 trachytic in composition, with the exception of Fe-Mn granitic glasses Log fO_2 -5.1 and -6.3, which are
279 tephriphonolite and trachyandesite, respectively. The Fe-Mn granitic glass Log fO_2 -6.3 is deficient in
280 Na_2O and K_2O compared to the other samples. All samples were synthesised at the same temperature
281 and left to dwell for the same time. Therefore, the difference in composition is likely to reflect a larger
282 surface area to bead volume for this sample.

283 1.7 X-ray absorption near edge structure spectroscopy

284

285 X-ray absorption near edge structure (XANES) spectra were collected for the PM1 composition
286 (samples NNO, Pt, PtC) to determine if any change in the oxidation state of Mn was detectable in
287 samples synthesised under different fO_2 conditions. Sample PtC should be much more reduced (NNO-
288 2.3, where $NNO \pm x$ refers to fO_2 relative to the Ni-NiO buffer in log 10 units), than both the Pt and
289 NNO samples, which are both expected to be more oxidised, around $NNO+0$, even accounting for any
290 uncertainties in the exact fO_2 at which samples were buffered. Spectra were obtained on both the
291 quenched glass and apatite crystals to determine any change in Mn oxidation state. The XANES spectra
292 from the quenched glass (Fig. 2) are remarkably similar in their shape, edge energy position and pre-
293 edge peak energy position between samples PM1 NNO, Pt and PtC suggesting there is very little/no
294 change in the oxidation state of Mn between these melts. When compared to tephroite ($Mn_2SiO_4 -$
295 Mn^{2+}) and $Mn_2O_3 (Mn^{3+})$ standards, the edge position is very close to the tephroite standard suggesting
296 Mn is in the 2+ oxidation state. There is no variation in the pre-edge peak position or intensity position
297 (Table 5) for these glasses. This suggests no major change in oxidation state or Mn coordination
298 between the quenched melts, with Mn incorporated exclusively, or almost exclusively, as Mn^{2+} .

299

300 XANES spectra for the PM1 apatite grains are also displayed in Figure 2. There are slight differences in
301 these 3 spectra with the position of the edge crest varying from a minimum of 6551.33eV for PM1 Pt,

302 6551.75eV for PM1 PtC and 6553.947 eV for PM1 NNO. This shift is thought to represent a change in
303 the local structure around Mn or an effect of crystal orientation (Dyar et al. 2002) rather than any
304 systematic changes in Mn mean oxidation state. A change in oxidation state is unlikely, as no
305 significant energy shift is observed in the pre-edge region (Table 5.), which is less sensitive to the
306 environment of the absorbing atom (Chalmin et al. 2009). Apatite spectra also suggest no major
307 change in Mn oxidation state between samples, with Mn dominantly present as Mn²⁺.

308

309 Additional XANES spectra were collected on Mn and Fe-Mn doped glasses from the HAP10
310 composition, which were synthesised under carefully controlled oxygen fugacities ($\log fO_2$ ranging
311 from -9.4 to -0.7 at 1300 °C) in a gas-mixing furnace. Mn pre-edge peak spectra for the Mn K-edge of
312 the glasses are shown in Figure 3A (Fe-Mn bearing glasses) and 3C (Mn glasses). Once again, there is
313 no observable shift in the Mn pre-edge peak energy as a function of fO_2 , suggesting that in all samples
314 Mn is in a similar valence and environment. The position of the intensity averaged centroid and the
315 location of the main edge suggest Mn²⁺ dominates in these silicate glasses. As there is no difference
316 between the Fe-free and Fe-bearing Mn spectra, this suggests that there is no reduction or oxidation
317 of the Mn³⁺ driven by redox changes in Fe during quench in the Fe-bearing samples. In contrast, the
318 Fe K-edge pre-edge peaks obtained from the same glass samples (Fig. 3B), show a clear shift in pre-
319 edge peak centroid to higher energy with more oxidising conditions. The oxidation state of Fe in the
320 Fe bearing glasses has been determined using the variogram diagram from Fiege et al. (2017), which
321 is based on the work of Wilke et al. (2001). Spectra collected on our glasses range from nearly 100%
322 Fe²⁺ (samples 66 and 76) down to a minimum of 22.8% Fe²⁺ (sample air/100; Fig. 4), and are consistent
323 with glasses in 5-fold, or a mix of 4- and 5-fold coordination.

324 Over the large range of fO_2 -T space explored for the high pressure and 1 atm. glasses we have been
325 unable to detect any measurable change in the oxidation state of Mn. XANES spectra instead imply
326 that Mn²⁺ dominates in all samples. The average oxidation state of Mn in apatite appears not to change

327 as a function of fO_2 -T conditions over the range of conditions used in this study. As such, we find no
328 evidence to support the assertion that variation of fO_2 in magmas should result in any significant
329 change in Mn valence.

330 Discussion

331 *Oxygen fugacity and D_{Mn}^{Ap-m}*

332

333 Our results demonstrate that the majority of Mn occurs as Mn^{2+} in melts across a range of fO_2
334 conditions. Here we test the empirical relationship defined by Miles et al. (2014; Fig. 5) by plotting
335 D_{Mn}^{Ap-m} (Nernst partition coefficient, $D_x = [x]_{\text{mineral}}/[x]_{\text{melt}}$) as a function of fO_2 . All samples in the SH3
336 haplo-basaltic composition show no significant variation in D_{Mn}^{Ap-m} as a function of fO_2 , even though
337 there is a variation of approximately 17 log units in fO_2 between samples. Similarly, there is no obvious
338 relationship between fO_2 and D_{Mn}^{Ap-m} for PM1 and Hap10 melt compositions. This suggests that
339 oxygen fugacity is not the main control on Mn apatite-melt partitioning in these compositions,
340 although significant variation in Mn partitioning is noted for experiments involving different melt
341 compositions. Samples in the BMT2 composition show an increase in D_{Mn}^{Ap-m} with decreasing fO_2 . This
342 is unlikely to be due to changes in the availability of Mn^{2+} in the melt (i.e. due to imposed fO_2) as the
343 XANES data indicates that the Mn^{2+}/Mn^{3+} ratio does not vary over a similar range in fO_2 to these
344 experiments. Instead, the apparent $fO_2 - D_{Mn}^{Ap-m}$ trend for BMT2 coincidentally corresponds to
345 changes in melt composition.

346 *Melt polymerisation and D_{Mn}^{Ap-m}*

347

348 It has long been recognised that trace element partition coefficients tend to be higher for minerals in
349 equilibrium with more silicic melts (Blundy and Wood 2003). Although this may partly reflect disparity
350 in the temperature and pressures of these systems it is thought the extent of melt polymerization is a
351 key control on element partitioning (Mahood and Stimac 1990; Schmidt et al. 2006). Polymerisation
352 is a measure of the extent to which silica tetrahedra within the melt structure are linked together. As

353 tetrahedral sites are linked together by shared oxygens (bridging oxygens), an increase in the extent
354 of polymerisation typically means a reduction in the ability of the melt to incorporate other elements.
355 Polymerisation of a melt can be compared in a variety of ways. In more felsic systems the aluminium
356 saturation index (ASI: molar ratio $\text{Al}_2\text{O}_3 / (\text{Na}_2\text{O} + \text{K}_2\text{O} + \text{CaO})$) provides an indication of melt
357 polymerisation (Prowatke and Klemme 2005). However, the ratio of non-bridging oxygens (NBO) to
358 tetrahedrally coordinated cations (T) is becoming the standard indicator of melt polymerisation
359 (Cottrell et al. 2009). $\text{NBO}/\text{T} = 0$ represents a fully polymerized melt, whereas 4 represents a fully
360 depolymerised melt of isolated tetrahedral (Kohn and Schofield 1994). Here NBO/T was calculated
361 using the procedure originally documented by Mysen et al. (1982, 1984). All Fe has been assigned as
362 network modifiers, due to lack of information on $\text{Fe}^{3+}/\text{Fe}^{\text{T}}$ in these samples.

363 Figure 6 displays the relationships between $D_{\text{Mn}}^{\text{Ap-m}}$ with NBO/T (Fig. 6A) and ASI (Fig. 6B) for samples
364 reported here and equivalent literature studies. ASI data from McCubbin et al. (2015) have not been
365 included given the absence of K_2O in their compositions. Both ASI and NBO/T parameters are
366 intrinsically linked, but there appears to be a stronger relationship between NBO/T and D_{Mn} than ASI,
367 indicating that melt polymerisation is more important than aluminosity in controlling Mn apatite-melt
368 partitioning. The partitioning of Mn into apatite in more polymerised melts appears to be considerably
369 greater than in more depolymerised melts, implying that melt structure has a strong influence on the
370 partitioning of Mn between apatite and melt. We would expect NBO/T to play a key role in dictating
371 $D_{\text{Mn}}^{\text{Ap-m}}$ over a range of melt compositions which are hosts of terrestrial apatite. Other parameters
372 which could influence $D_{\text{Mn}}^{\text{Ap-m}}$ are temperature and pressure. However, a similar relationship with
373 $D_{\text{Mn}}/D_{\text{Zn}}$ (olivine-melt) and NBO/T was documented by Kohn and Schofield (1994), who also
374 demonstrated that melt composition has a stronger effect on mineral-melt partitioning than
375 temperature.

376 The relationship of NBO/T with $D_{\text{Mn}}^{\text{Ap-m}}$ may arise if Mn ions are coordinated with non-bridging
377 oxygens in silicate melts (Watson 1977). In more polymerised melts, the availability of non-bridging

378 oxygens is lower, and therefore, the extent to which melt networks incorporate metal cations such
379 as Mn^{2+} will be reduced. Alternatively, the observed relationship can be explained based on Mn^{2+}
380 interaction with melt networks, where Mn-O bonding in more polymerised melts is less favourable
381 due to the destabilising effect it has on the silicate framework (Kohn and Schofield 1994). It is unlikely
382 that the high D_{Mn}^{Ap-m} are due to the octahedral site preference energy of the Mn^{2+} ion, as Mn^{2+} has an
383 octahedral site preference energy of zero because of the ion's d^5 electron configuration (Kohn and
384 Schofield 1994).

385 *Mn content of apatite at Criffel pluton*

386

387 Miles et al. (2014) highlighted that variations in the Mn content of apatite from different zones within
388 the Criffell granitic pluton (southern Scotland) appeared to correlate with changes in melt fO_2 , and
389 were relatively independent of other parameters such as temperature and the concentration of Mn
390 in the melt. As the partitioning data presented here indicates there is no relationship between D_{Mn}^{Ap-}
391 m and fO_2 we used the range of compositions from our study to test other hypotheses. If we apply the
392 NBO/T to D_{Mn}^{Ap-m} power relationship given in Figure 6 to the data for the Criffel pluton, we can
393 determine apparent D_{Mn}^{Ap-m} for the relevant melt compositions. NBO/T was calculated from whole
394 rock compositions (Stephens and Halliday 1980; Miles et al. 2013) for the 4 petrologically distinct
395 zones of the pluton for which apatite Mn concentrations were available (Miles et al. 2014). These
396 compositions have been chosen to obtain the largest change in NBO/T. Whole rock MnO contents
397 were combined with the modelled D_{Mn}^{Ap-m} based on NBO/T to predict apatite MnO, and then data was
398 converted to ppm for comparison. This method predicts a reasonable fit of the Mn apatite content
399 (ppm) based on NBO/T with measured apatite concentrations from EPMA and SIMS data (Miles et al.
400 2014; Fig. 7). The error in Figure 7 is large indicating the sensitivity of apatite Mn content to the power
401 law fit. The predicted Mn apatite content is also very sensitive to the modelled bulk rock composition
402 and bulk rock MnO content. However, to a first approximation, it appears that the variation seen in
403 apatite Mn concentration at Criffel can be explained solely by variations in NBO/T rather than fO_2 . This

404 is, perhaps, unsurprising as XANES work indicates that over the range of fO_2 conditions inferred for
405 this pluton there is no change in the oxidation state of Mn^{2+} in silicate melt.

406

407 *Volatile partitioning as a function of melt structure and oxygen fugacity*

408

409 Manganese is unlikely to be the only element for which apatite-melt partitioning is affected by melt
410 composition. Aside from the effect which melt polymerisation should have on partitioning of other
411 cations readily incorporated onto octahedral sites in silicate melt structure, partitioning of anions
412 between apatite and melt may also be affected by NBO/T. Figure 8 shows that D_{Cl}^{Ap-m} is also linked to
413 melt structure for dominantly hydroxyapatite compositions ($X_{H_2O}^{Ap} > 0.5$ a.p.f.u.). In Figure 8, data
414 from this study as well as Doherty et al. (2014) and Prowatke and Klemme (2006), all show an increase
415 in D_{Cl}^{Ap-m} with increasing polymerisation of the melt. This is similar to the trend noted for D_{Mn}^{Ap-m} , with
416 Cl becoming more incompatible in the melt with higher degrees of melt polymerisation. This may be
417 because the most polymerised melts also have lower wt% of Ca, Fe, Na and Mg, which are species
418 known to enhance the solubility of Cl in silicate melts (Mathez and Webster 2009).

419 It has been argued that Nernst partition coefficients are not suitable when examining the distribution
420 of halogens and water between apatite and melt (Boyce et al., 2014; McCubbin et al., 2015) as the
421 combined concentration of Cl, F and OH in the apatite structure is fixed based on stoichiometry
422 (McCubbin et al. 2015). A more suitable measure of volatile partitioning in apatite is the exchange
423 coefficient, K_D (Eq. 2). Equation 2 describes the exchange of OH-F between apatite and melt:

424
$$K_D^{OH-F} = \frac{\left(\frac{OH_{ap}}{OH_m}\right)}{\left(\frac{F_{ap}}{F_m}\right)} = \frac{\left(\frac{OH_{ap}}{F_{ap}}\right)}{\left(\frac{OH_m}{F_m}\right)} \quad [2]$$

425 The exchange coefficient allows partitioning behaviour of two major elements competing for the same
426 crystallographic site to be determined. The exchange coefficient treats F, Cl and H, as major elements,
427 and models them in a similar fashion to the behaviour of Mg and Fe between olivine and melt (Roeder

428 and Emslie 1970). Assuming ideal behaviour, K_D can be calculated using the mole fraction or wt. % of
429 each species.

430 As such, instead of examining the relationship of D_{Cl}^{Ap-m} with NBO/T, a more suitable parameter may
431 be $K_D^{Cl-H_2O}$. However, $K_D^{Cl-H_2O}$ data from published literature for apatite of this composition is much
432 more restricted, making it difficult to determine if there is a relationship with NBO/T.

433 In contrast, D_F^{Ap-m} appears to be unaffected by melt composition for runs carried out in the fluorapatite
434 end member composition, likely reflecting that F behaves slightly different in the melt structure to Cl,
435 or that partitioning of F is more dependent on apatite crystal chemistry, and therefore less affected
436 by melt composition.

437 Throughout the entire dataset there is no obvious influence of fO_2 on partitioning/exchange of the
438 anions. Therefore, it is likely that mineral-melt partitioning of these elements is controlled by
439 additional variables, such as, element availability in the melt, temperature, and structural controls
440 from apatite and melt.

441

442

443 Conclusions

444 Apatite-silicate melt partitioning experiments described here demonstrate that fO_2 has no discernible
445 influence on Mn or volatile partitioning. This is consistent with the results of XANES spectroscopy
446 which demonstrate that over a wide range of fO_2 conditions Mn is incorporated into both apatite and
447 a range of silicate melts as Mn^{2+} . Instead, results of this study, combined with literature data show
448 that melt structure, and in particular the extent of melt polymerization as defined by the ratio NBO/T,
449 controls partitioning of Mn between apatite and a range of silicate melts. The varying Mn content of
450 apatite from the Criffel pluton can be explained by the varying degrees of melt polymerisation for
451 samples from different zones of the pluton, rather than changes in the oxygen fugacity of the parental

452 magma, as previously suggested. More polymerised melts generally have a much higher mineral-melt
453 partition coefficient for trace elements (e.g. Mn apatite-melt), than corresponding, less polymerised
454 melts. Therefore, empirical relationships between variables such as oxygen fugacity and the Mn
455 content in apatite are not valid across systems where melt composition changes, and further terms in
456 such equations are needed to constrain the influence of melt composition.

457 Acknowledgements

458 The project was funded by the Natural Environment Research Council as part of a NERC E³ DTP
459 studentship (NERC grant NE/L002558/1), as well as analytical time at the NERC ion microprobe facility.
460 Additional funding was granted from the Daniel Pidgeon fund – The Geological Society. XANES data
461 was acquired at the Diamond Light Source, grant sp12876-1. We thank Stuart Kearns and Ben Buse for
462 analytical support at the University of Bristol, and Richard Hinton for his expertise and guidance at the
463 NERC ion microprobe facility. The authors thank Professor James Brenan, whose detailed review
464 improved this manuscript.

465 References Cited

- 466 Belousova, E.A., Walters, S., Griffin, W.L., and O'Reilly, S.Y. (2001) Trace-element signatures of
467 apatites in granitoids from the Mt Isa Inlier, northwestern Queensland. *Australian Journal of*
468 *Earth Sciences*, 48, 603–619.
- 469 Blundy, J., and Wood, B. (2003) Partitioning of trace elements between crystals and melts. *Earth and*
470 *Planetary Science Letters*, 210, 383–397.
- 471 Boyce, J.W., Tomlinson, S.M., McCubbin, F.M., Greenwood, J.P., and Treiman, A.H. (2014) The lunar
472 apatite paradox. *Science*, 344, 400–402.
- 473 Brounce, M., Kelley, K.A., Cottrell, E., and Reagan, M.K. (2015) Temporal evolution of mantle wedge
474 oxygen fugacity during subduction initiation. *Geology*, 43, 775–778.
- 475 Burnham, A. D., Berry, A. J., Halse, H. R., Schofield, P. F., Cibin, G., & Mosselmans, J. F. W. (2015). The

476 oxidation state of europium in silicate melts as a function of oxygen fugacity, composition and
477 temperature. *Chemical Geology*, 411, 248–259.

478 Cottrell, E., Walter, M. J., & Walker, D. (2009). Metal-silicate partitioning of tungsten at high pressure
479 and temperature: Implications for equilibrium core formation in Earth. *Earth and Planetary
480 Science Letters*, 281(3–4), 275–287.

481 Chalmin, E., Farges, F. & Brown, G.E. (2009). A pre-edge analysis of Mn K-edge XANES spectra to help
482 determine the speciation of manganese in minerals and glasses. *Contributions to Mineralogy
483 and Petrology*, 157, 111-126

484 Chu, M.-F., Wang, K.-L., Griffin, W.L., Chung, S.-L., O'Reilly, S.Y., Pearson, N.J., and Iizuka, Y. (2009)
485 Apatite Composition: Tracing Petrogenetic Processes in Transhimalayan Granitoids. *Journal of
486 Petrology*, 50, 1829.

487 Dai, L., and Karato, S. (2014) Influence of oxygen fugacity on the electrical conductivity of hydrous
488 olivine: Implications for the mechanism of conduction. *Physics of the Earth and Planetary
489 Interiors*, 232, 57–60.

490 Doherty, A. L., Webster, J. D., Goldoff, B. A., & Piccoli, P. M. (2014). Partitioning behavior of chlorine
491 and fluorine in felsic melt-fluid(s)-apatite systems at 50MPa and 850-950 °C. *Chemical Geology*,
492 384, 94–109.

493 Douce, A.E.P., and Roden, M. (2006) Apatite as a probe of halogen and water fugacities in the
494 terrestrial planets. *Geochimica et Cosmochimica Acta*, 70, 3173–3196.

495 Dyar, M. D., Gunter, M. E., Delaney, J. S., Lanzirotti, A., & Sutton, S. R. (2002). Use of the spindle
496 stage for orientation of single crystals for microXAS: Isotropy and anisotropy in Fe-XANES
497 spectra. *American Mineralogist*, 87(10), 1500–1504

498 Eugster, H. P. (1957). Heterogeneous Reactions Involving Oxidation and Reduction at High Pressures
499 and Temperatures. *The Journal of Chemical Physics*, 26(6), 1760–1761.

500 Eugster, H. P., & Wones, D. R. (1962). Stability Relations of the Ferruginous Biotite, Annite. *Journal of*
501 *Petrology*, 3(1), 82–125.

502 Fiege, A., Ruprecht, P., Simon, A. C., Bell, A. S., Göttlicher, J., Newville, M., ... Moore, G. (2017).
503 Calibration of Fe XANES for high-precision determination of Fe oxidation state in glasses:
504 Comparison of new and existing results obtained at different synchrotron radiation sources.
505 *American Mineralogist*, 102(2), 369–380.

506 Fleet, M.E., Stone, W.E., and Crocket, J.H. (1991) Partitioning of palladium, iridium, and platinum
507 between sulfide liquid and basalt melt: Effects of melt composition, concentration, and oxygen
508 fugacity. *Geochimica et Cosmochimica Acta*, 55, 2545–2554.

509 Gross, J., Filiberto, J., and Bell, A.S. (2013) Water in the martian interior: Evidence for terrestrial
510 MORB mantle-like volatile contents from hydroxyl-rich apatite in olivine–phyric shergottite
511 NWA 6234. *Earth and Planetary Science Letters*, 369–370, 120–128.

512 Haskel, D. (1999). FLUO: Correcting XANES for self-absorption in fluorescence measurements.

513 Hensen, B.J. (1986) Theoretical phase relations involving cordierite and garnet revisited: the
514 influence of oxygen fugacity on the stability of sapphirine and spinel in the system Mg-Fe-Al-Si-
515 O. *Contributions to Mineralogy and Petrology*, 92, 362–367.

516 Holzheid, A., & O'Neill, H. S. C. (1995). The Cr-Cr₂O₃ oxygen buffer and the free energy of formation
517 of Cr₂O₃ from high-temperature electrochemical measurements. *Geochimica et cosmochimica*
518 *acta*, 59(3), 475-479.

519 Hughes, J.M. (2015) The many facets of apatite. *American Mineralogist*, 100, 1033–1039.

520 Hughes, J.M., Ertl, A., Bernhardt, H.-J., Rossman, G.R., and Rakovan, J. (2004) Mn-rich fluorapatite
521 from Austria: Crystal structure, chemical analysis, and spectroscopic investigations. *American*
522 *Mineralogist*, 89, 629–632.

523 Jacobsson, E. (1985). Solid State EMF Studies of the Systems FeO--Fe₃O₄ and Fe₃O₄--Fe₂O₃ in the
524 Temperature Range 1000-1600 K. *Scandinavian Journal of Metallurgy.*, 14(5), 252-256.

525 Jakobsson, S. (2012). Oxygen fugacity control in piston-cylinder experiments. *Contributions to*
526 *Mineralogy and Petrology*, 164(3), 397–406

527 Kasting, J.F., Egglar, D.H., and Raeburn, S.P. (1993) Mantle Redox Evolution and the Oxidation State
528 of the Archean Atmosphere. *The Journal of Geology*, 101, 245–257.

529 Kohn, S.C., and Schofield, P.F. (1994) The importance of melt composition in controlling trace-
530 element behaviour: an experimental study of Mn and Zn partitioning between forsterite and
531 silicate melts. *Chemical Geology*, 117, 73–87.

532 Konecke, B.A., Fiege, A., Simon, A.C., Parat, F., and Stechern, A. (2017) Co-variability of S₆₊ , S₄ + ,
533 and S₂ – in apatite as a function of oxidation state : Implications for a new oxybarometer.
534 *American Mineralogist*, 102, 548–557.

535 Kump, L.R., Kasting, J.F., and Barley, M.E. (2001) Rise of atmospheric oxygen and the “upside-down”
536 Archean mantle. *Geochemistry, Geophysics, Geosystems*, 2, n/a--n/a.

537 Li, J., & Agee, C. B. (2001). The effect of pressure, temperature, oxygen fugacity and composition on
538 partitioning of nickel and cobalt between liquid Fe-Ni-S alloy and liquid silicate: Implications for
539 the Earth’s core formation. *Geochimica et Cosmochimica Acta*, 65(11), 1821–1832.

540 Mahood, G. A., & Stimac, J. A. (1990). Trace-element partitioning in pantellerites and trachytes.
541 *Geochimica et Cosmochimica Acta*, 54(8), 2257–2276.

542 Matjuschkin, V., Brooker, R. A., Tattitch, B., Blundy, J. D., & Stamper, C. C. (2015). Control and
543 monitoring of oxygen fugacity in piston cylinder experiments. *Contributions to Mineralogy and*
544 *Petrology*, 169(1), 9.

545 Marks, M. A. W., Scharrer, M., Ladenbuerger, S. and Markl, G.. Comment on “Apatite: A new redox

546 proxy for silicic magmas?" by Miles A.J., Graham C.M., Hawkesworth C., Gillespie M.R., Hinton
547 R.W., Bromiley G.D.. *Geochim. Cosmochim. Acta* (2016)

548 Mathez, E. A., & Webster, J. D. (2005). Partitioning behavior of chlorine and fluorine in the system
549 apatite-silicate melt-fluid. *Geochimica et Cosmochimica Acta*, 69(5), 1275–1286.

550 McCubbin, F.M., Vander Kaaden, K.E., Tartèse, R., Boyce, J.W., Mikhail, S., Whitson, E.S., Bell, A.S.,
551 Anand, M., Franchi, I.A., Wang, J., and others (2015) Experimental investigation of F, Cl, and OH
552 partitioning between apatite and Fe-rich basaltic melt at 1.0-1.2 GPa and 950-1000 °C.
553 *American Mineralogist*, 100, 1790–1802.

554 McCubbin, F.M., Boyce, J.W., Srinivasan, P., Santos, A.R., Elardo, S.M., Filiberto, J., Steele, A., and
555 Shearer, C.K. (2016) Heterogeneous distribution of H₂O in the Martian interior: Implications for
556 the abundance of H₂O in depleted and enriched mantle sources. *Meteoritics and Planetary
557 Science*, 51, 2036–2060.

558 Médard, E., McCammon, C.A., Barr, J.A., and Grove, T.L. (2008) Oxygen fugacity, temperature
559 reproducibility, and H₂O contents of nominally anhydrous piston-cylinder experiments using
560 graphite capsules. *American Mineralogist*, 93, 1838–1844.

561 Miles, A. J., Graham, C. M., Hawkesworth, C. J., Gillespie, M. R., & Hinton, R. W. (2013). Evidence for
562 distinct stages of magma history recorded by the compositions of accessory apatite and zircon.
563 *Contributions to Mineralogy and Petrology*, 166(1), 1–19. [https://doi.org/10.1007/s00410-013-](https://doi.org/10.1007/s00410-013-0862-9)
564 [0862-9](https://doi.org/10.1007/s00410-013-0862-9)

565 Miles, A.J., Graham, C.M., Hawkesworth, C.J., Gillespie, M.R., Hinton, R.W., and Bromiley, G.D. (2014)
566 Apatite: A new redox proxy for silicic magmas? *Geochimica et Cosmochimica Acta*, 132, 101–
567 119.

568 Mosselmans, J. F. W., Quinn, P. D., Dent, A. J., Cavill, S. A., Moreno, S. D., Peach, A., Leicester, P. J.,
569 Keylock, S. J., Gregory, S. R., Atkinson, K. D. & Rosell, J. R. (2009). *J. Synchrotron Rad.* 16, 818-

570 824.

571 Moussallam, Y., Edmonds, M., Scaillet, B., Peters, N., Gennaro, E., Sides, I., and Oppenheimer, C.
572 (2016) The impact of degassing on the oxidation state of basaltic magmas: A case study of
573 Kīlauea volcano. *Earth and Planetary Science Letters*, 450, 317–325.

574 Mysen, B. O., Virgo, D., & Seifert, F. A. (1982). The structure of silicate melts: implications for
575 chemical and physical properties of natural magma. *Reviews of Geophysics*, 20(3), 353-383.

576 Mysen, B. O., Virgo, D., & Seifert, F. A. (1984). Redox equilibria of iron in alkaline earth silicate melts;
577 relationships between melt structure, oxygen fugacity, temperature and properties of iron-
578 bearing silicate liquids. *American Mineralogist*, 69(9-10), 834-847.

579 Nagasawa, H. (1970) Rare earth concentrations in zircons and apatites and their host dacites and
580 granites. *Earth and Planetary Science Letters*, 9, 359–364.

581 O'Neill, H. S. C. (1988). Systems Fe-O and Cu-O: thermodynamic data for the equilibria Fe-'FeO', Fe-
582 Fe₃O₄, 'FeO'-Fe₃O₄, Fe₃O₄-Fe₂O₃, Cu-Cu₂O, and Cu₂O-CuO from emf measurements. *Amer.*
583 *Mineral*, 73, 470-486.

584 O'Neill, H. S. C., & Pownceby, M. I. (1993). Thermodynamic data from redox reactions at high
585 temperatures. I. An experimental and theoretical assessment of the electrochemical method
586 using stabilized zirconia electrolytes, with revised values for the Fe-"FeO", Co-CoO, Ni-NiO and
587 Cu-Cu₂O oxygen buffers, and new data for the W-WO₂ buffer. *Contributions to Mineralogy and*
588 *Petrology*, 114(3), 296-314.

589 Prowatke, S., and Klemme, S. (2005) Effect of melt composition on the partitioning of trace elements
590 between titanite and silicate melt. *Geochimica et Cosmochimica Acta*, 69, 695–709.

591 Ravel, B., & Newville, M. (2005). ATHENA, ARTEMIS, HEPHAESTUS: data analysis for X-ray absorption
592 spectroscopy using IFFFIT. *Journal of Synchrotron Radiation*, 12(4), 537–541.

593 Riker, J., Humphreys, M. C. S., Brooker, R. A., & De Hoog, J. C. M. (2018). First measurements of OH-C

594 exchange and temperature-dependent partitioning of OH and halogens in the system apatite–
595 silicate melt. *American Mineralogist*, 103(2), 260–270.

596 Roeder, P. L., and Emslie, R. (1970). Olivine-liquid equilibrium. *Contributions to mineralogy and*
597 *petrology*, 29(4), 275-289.

598 Ryerson, F.J., Durham, W.B., Cherniak, D.J., and Lanford, W.A. (1989) Oxygen diffusion in olivine:
599 Effect of oxygen fugacity and implications for creep. *Journal of Geophysical Research: Solid*
600 *Earth*, 94, 4105–4118.

601 Scaillet, B., and Gaillard, F. (2011) Redox state of early magmas. *Nature*, 480, 48–49.

602 Schmidt, M. W., Connolly, J. A. D., Günther, D., & Bogaerts, M. (2006). Element partitioning: The role
603 of melt structure and composition. *Science*, 312(5780), 1646–1650.

604 Scott, J.A.J., Humphreys, M.C.S., Mather, T.A., Pyle, D.M., and Stock, M.J. (2015) Insights into the
605 behaviour of S, F, and Cl at Santiaguito Volcano, Guatemala, from apatite and glass. *Lithos*, 232,
606 375–394.

607 Sha, L.-K., and Chappell, B.W. (1999) Apatite chemical composition, determined by electron
608 microprobe and laser-ablation inductively coupled plasma mass spectrometry, as a probe into
609 granite petrogenesis. *Geochimica et Cosmochimica Acta*, 63, 3861–3881.

610 Shannon, R. D. (1976). Revised effective ionic radii and systematic studies of interatomic distances in
611 halides and chalcogenides. *Acta Crystallographica Section A*, 32(5), 751–767.

612 Stephens, W.E., and Halliday, A.N. (1980) Discontinuities in the composition surface of a zoned
613 pluton, Criffell, Scotland. *GSA Bulletin*, 91, 165–170.

614 Toplis, M.J., and Carroll, M.R. (1995) An Experimental Study of the Influence of Oxygen Fugacity on
615 Fe-Ti Oxide Stability, Phase Relations, and Mineral—Melt Equilibria in Ferro-Basaltic Systems.
616 *Journal of Petrology*, 36, 1137.

- 617 Trail, D., Watson, E.B., and Tailby, N.D. (2011) The oxidation state of Hadean magmas and
618 implications for early Earth's atmosphere. *Nature*, 480, 79–82.
- 619 Wallace, P., and Carmichael, I.S.E. (1992) Sulfur in basaltic magmas. *Geochimica et Cosmochimica*
620 *Acta*, 56, 1863–1874.
- 621 Watson, E. B. (1977). Partitioning of manganese between forsterite and silicate liquid. *Geochimica et*
622 *Cosmochimica Acta*, 41(9), 1363–1374.
- 623 Watson, E., Wark, D., Price, J., & Van Orman, J. (2002). Mapping the thermal structure of solid-
624 media pressure assemblies. *Contributions to Mineralogy and Petrology*, 142(6), 640–652.
- 625 Webster, J. D., Tappen, C. M., & Mandeville, C. W. (2009). Partitioning behavior of chlorine and
626 fluorine in the system apatite–melt–fluid. II: Felsic silicate systems at 200 MPa. *Geochimica et*
627 *Cosmochimica Acta*, 73(3), 559–581.
- 628 Wilke, M., Farges, F., Petit, P.-E., Brown, G. E., & Martin, F. (2001). Oxidation state and coordination
629 of Fe in minerals: An Fe K-XANES spectroscopic study. *American Mineralogist*, 86(5–6), 714–730
- 630 Wojdyr, M. (2010) Fityk: a general-purpose peak fitting program. *Journal of Applied Crystallography*,
631 43, 1126–1128.
- 632 Wood, B.J., and Nell, J. (1991) High-temperature electrical conductivity of the lower-mantle phase
633 (Mg, Fe)O. *Nature*, 351, 309.
- 634 Yang, X., Gaillard, F., & Scaillet, B. (2014). A relatively reduced Hadean continental crust and
635 implications for the early atmosphere and crustal rheology. *Earth and Planetary Science*
636 *Letters*, 393, 210–219.

637

638

639

640 **Figure captions**

641 **Figure 1:** Total alkali-silica (TAS) plot for quenched melt compositions. Sample names refer to oxygen
642 fugacity buffer and starting bulk composition used in each run, see text and table 2 for details.

643 **Figure 2: (A)** Stacked XANES spectra for PM1- Pt (solid green line), PtC (solid red line), and NNO glasses
644 (solid purple line) (B) focus on the pre-edge region of A. (C) Stacked XANES spectra of PM1- Pt (solid
645 green line), PtC (solid red line) and NNO (solid purple line) apatite (D) focus on pre-edge peaks of C.
646 Also plotted on A) and C) is an additional XANES spectrum of PM1 Pt with the spectra for the standards
647 tephroite ($\text{Mn}_2\text{SiO}_4 - \text{Mn}^{2+}$) (solid black line) and $\text{Mn}_2\text{O}_3 (\text{Mn}^{3+})$ (dashed black line).

648 **Figure 3:** (A) Mn K-edge, (B) Fe K-edge spectra acquired on the same set of Fe-Mn doped granitic glass,
649 and (C) Mn K-edge spectra from Mn doped granitic glass. For reference $\log f\text{O}_2$ of NNO = -6.5 at 1300 °C.

650 **Figure 4:** Variogram (Wilke et al. 2001) that shows the average centroid position and integrated pre-
651 edge intensity for Fe reference compounds in single valence/single coordination (grey ellipses and
652 black dots). The black dotted lines indicate binary mixes between the end member reference
653 compounds. Also plotted are the centroid position and intensity for the Fe-Mn doped granitic glasses
654 from this study (crosses). For reference $\log f\text{O}_2$ of NNO = -6.5 at 1300 °C.

655 **Figure 5:** $D_{\text{Mn}}^{\text{Ap-m}}$ plotted as a function of $\log f\text{O}_2$ for apatite-melt partitioning experiments from this
656 study.

657 **Figure 6:** $D_{\text{Mn}}^{\text{Ap-m}}$ plotted as a function of ASI (Aluminium saturation index) and NBO/T (number of
658 nonbridging oxygen per tetrahedral cation) for samples in this study and those from Sha and Chappell
659 (1999), Belousova et al. (2001), and McCubbin et al. (2015). The power fit is fitted using data from this
660 study, McCubbin et al. (2015) and Sha and Chappell (1999). Belousova et al. (2001) data is not used
661 for the power law fit because although the data shows a similar trend to other studies, there is an
662 unexplained offset to lower NBO/T.

663 **Figure 7:** Boxplot of Mn apatite concentration (ppm) for the 4 petrologically distinct zones of the Criffel
664 Pluton (Miles et al. 2014). The blue box highlights the interquartile range for the dataset, with the blue
665 line indicating the median value. The black whiskers represent the range of the dataset. Overlaying
666 this data is the apparent Mn apatite concentration (red crosses) determined from the power law
667 relationship between NBO/T and $D_{\text{Mn}}^{\text{Ap-m}}$ shown in Fig. 6, and associated error (red lines) based on the
668 90% confidence intervals.

669 **Figure 8:** $D_{\text{Cl}}^{\text{Ap-m}}$ against melt NBO/T for our study and literature data (Mathez and Webster 2005;
670 Webster et al. 2009; Doherty et al. 2014).

671

1 **Table 1:** Target melt compositions, wt% oxide, without additional apatite component. Added to each bulk composition was a 7:3 of starting material to
2 apatite component, consisting of 1.5 mol $\text{Ca}_3(\text{PO}_4)_2$ to either 1 mol. CaCl_2 (PM1/HAP10/HAP5) or 1 mol. CaF_2 (BMT2/SH3). H_2O added in the form of brucite
3 or gibbsite

4

5

	PM1	HAP10	HAP5	BMT2	SH3
SiO₂	64.1	63.7	72.2	61.3	52.2
TiO₂	-	-	-	0.4	-
Al₂O₃	17.1	17.1	13.4	18.4	17.3
FeO	-	-	-	3.1	-
MnO	7.4	7.3	5.3	1.0	1.0
MgO	-	-	-	0.2	11.5
CaO	-	-	-	0.9	12.1
Na₂O	4.7	4.7	5.4	6.1	2.7
K₂O	6.8	7.2	3.7	7.0	1.8
H₂O*	-	-	-	1.5	1.5

6

7 **Table 2:** Experimental parameters, and average major and trace element composition of melt for experimental runs. Errors represent 1 σ . Duration relates
8 to hours at final T, while ramp rate is degrees cooled per hour. Note: Pt = single Pt capsule, H= single Pt capsule with added H₂O, NNO = Ni-NiO buffer, MH =
9 Fe₃O₄-Fe₂O₃ buffer, MW = Fe₃O₄-FeO buffer, Cr = Cr-Cr₂O₃ buffer, PtC = graphite capsule inside Pt. H₂O measurements were made by SIMS. NBO/T = number
10 of non-bridging oxygen per tetrahedrally coordinated cation (see text for details).

	PM1 Pt	PM1 H	PM1 NNO	PM1 PtC	MH 1200 Hap10	MW 1200 Hap10	Cr 1200 Hap10	NNO 1200 Hap10	Cr 1200 Hap5
Initial T	1450	1450	1450	1450	1400	1400	1400	1400	1400
Final T	1250	1100	1250	1250	1200	1200	1200	1200	1200
Ramp Rate	60	60	60	60	60	60	60	60	60
Est. fO₂¹	-7.0	-8.8	-7.0	-9.9	-2.9	-9.3	-17.6	-7.6	-17.6
Duration	23	18	20	21	19	20	24	21	21
Glass									
SiO₂	53.39 ± 0.64	61.86 ± 0.78	52.38 ± 0.38	56.13 ± 0.68	50.07 ± 0.58	56.89 ± 1.11	53.48 ± 0.41	52.13 ± 0.51	63.00 ± 0.85
TiO₂									
Al₂O₃	14.40 ± 0.18	17.85 ± 0.27	15.51 ± 0.20	16.08 ± 0.18	14.60 ± 0.16	16.11 ± 0.17	15.18 ± 0.15	15.41 ± 0.41	12.93 ± 0.13
FeO^T					1.66 ± 0.12	1.57 ± 0.09	0.03 ± 0.01		
MgO					0.10 ± 0.01	0.25 ± 0.02	0.07 ± 0.01	0.08 ± 0.01	0.08 ± 0.01
MnO	9.21 ± 0.52	4.31 ± 0.34	9.06 ± 0.32	6.69 ± 0.27	7.57 ± 0.31	7.16 ± 0.53	7.18 ± 0.22	7.65 ± 0.33	3.88 ± 0.03
CaO	6.10 ± 0.27	1.71 ± 0.08	4.56 ± 0.11	4.43 ± 0.13	4.05 ± 0.19	3.27 ± 0.29	3.32 ± 0.09	4.61 ± 0.23	2.58 ± 0.08
K₂O	5.14 ± 0.13	6.67 ± 0.10	4.45 ± 0.07	4.85 ± 0.1	5.20 ± 0.10	6.22 ± 0.16	5.54 ± 0.12	5.47 ± 0.13	3.48 ± 0.08
Na₂O	5.21 ± 0.14	5.45 ± 0.07	2.51 ± 0.09	3.38 ± 0.13	3.32 ± 0.19	4.03 ± 0.12	3.68 ± 0.26	3.68 ± 0.25	4.57 ± 0.13
P₂O₅	3.46 ± 0.23	0.82 ± 0.07	2.85 ± 0.12	1.76 ± 0.11	3.62 ± 0.40	2.12 ± 0.08	2.70 ± 0.20	3.41 ± 0.32	2.20 ± 0.02
Cl	2.45 ± 0.13	0.47 ± 0.03	0.29 ± 0.03	2.08 ± 0.11	0.46 ± 0.01	0.22 ± 0.01	0.15 ± 0.00	0.56 ± 0.05	0.08 ± 0.01
F									
Total	99.35 ± 0.29	99.14 ± 0.99	91.6 ± 0.48	95.39 ± 0.52	90.71 ± 0.89	97.91 ± 0.45	91.39 ± 0.39	93.27 ± 0.87	92.93 ± 0.89
H₂O	0.92		7.79	2.78	7.97		7.63	5.60	6.44
CO₂	0.16		0.11	0.03				0.20	
NBO/T	0.43	0.12	0.27	0.21	0.29	0.24	0.25	0.30	0.15

12 Table 2 continued

	SH3 Cr	SH3 PtC	SH3 Pt	SH3 MH	BMT2 Cr	BMT2 Pt	BMT2 MH
Initial T	1400	1400	1400	1400	1500	1500	1500
Final T	1250	1250	1250	1250	1350	1350	1350
Ramp Rate	60	60	60	60	10	10	10
Est. fO₂¹	-16.76	-9.91	-7.00	-2.32	-15.20	-6.00	-1.28
Duration	24	24	24	24	9	9	9
Glass							
SiO₂	46.47 ± 0.43	46.36 ± 0.45	45.78 ± 0.43	45.42 ± 0.50	60.56 ± 0.45	55.80 ± 0.63	45.38 ± 0.49
TiO₂					0.27 ± 0.04	0.30 ± 0.02	0.25 ± 0.01
Al₂O₃	15.64 ± 0.18	15.59 ± 0.18	15.47 ± 0.01	15.33 ± 0.11	18.45 ± 0.09	17.49 ± 0.09	13.34 ± 0.21
FeO^T		0.04 ± 0.01		1.75 ± 0.05		1.29 ± 0.05	12.08 ± 0.20
MgO	10.00 ± 0.07	10.18 ± 0.06	10.00 ± 0.05	8.55 ± 0.07	0.32 ± 0.01	0.30 ± 0.01	0.28 ± 0.01
MnO	0.73 ± 0.02	0.79 ± 0.02	0.90 ± 0.01	0.86 ± 0.01	0.07 ± 0.01	0.76 ± 0.01	0.58 ± 0.01
CaO	16.47 ± 0.20	16.46 ± 0.06	16.16 ± 0.30	15.56 ± 0.05	3.60 ± 0.03	4.31 ± 0.12	8.11 ± 0.13
K₂O	1.58 ± 0.05	1.58 ± 0.06	1.49 ± 0.05	1.66 ± 0.02	6.97 ± 0.09	6.27 ± 0.08	5.09 ± 0.08
Na₂O	2.62 ± 0.13	2.42 ± 0.14	2.51 ± 0.17	2.66 ± 0.14	6.34 ± 0.17	5.73 ± 0.26	4.76 ± 0.26
P₂O₅	4.15 ± 0.12	3.99 ± 0.03	4.19 ± 0.01	4.03 ± 0.02	1.35 ± 0.05	2.48 ± 0.08	5.74 ± 0.18
Cl							
F	1.35 ± 0.05	1.36 ± 0.05	1.37 ± 0.03	1.28 ± 0.08	1.00 ± 0.06	1.07 ± 0.08	1.22 ± 0.07
Total	99.07 ± 0.48	98.78 ± 0.45	97.90 ± 0.20	97.11 ± 0.65	99.09 ± 0.25	95.78 ± 0.37	96.88 ± 0.51
H₂O	1.60	0.89	1.89	1.89	0.48	2.07	1.90
CO₂	0.69	0.29					
NBO/T	0.86	0.86	0.86	0.79	0.11	0.15	0.36

13

14 ¹fO₂ estimated based on a_{H₂O}=1; for all double capsule experiments it is possible that fO₂ is lower due to reduced a_{H₂O}.

15 **Table 3: Major and trace element compositions of apatite, and associated partition coefficients for**
 16 **experimental runs.** Errors represent 1 σ . Note: Pt = single Pt capsule, H= single Pt capsule with added
 17 H₂O, NNO =Ni-NiO buffer, MH = Fe₃O₄-Fe₂O₃ buffer, MW = Fe₃O₄-FeO buffer,Cr = Cr-Cr₂O₃ buffer, PtC
 18 = graphite capsule inside Pt. H₂O measurements were made by SIMS. X^{Ap}F = F^{Ap}/3.767, X^{Ap}Cl =
 19 Cl^{Ap}/6.809 and X^{Ap}H₂O = H₂O^{Ap}/1.81. Structural formulas are calculated based on 26 anions.

	PM1 Pt	PM1 H	PM1 NNO	PM1 C	MH 1200 Hap10
# Analyses	17	20	28	19	9
SiO ₂	0.37 ± 0.06	0.48 ± 0.10	0.27 ± 0.05	0.45 ± 0.05	0.18 ± 0.01
Al ₂ O ₃	0.04 ± 0.01	0.06 ± 0.02		0.06 ± 0.03	
FeO ^T					0.14 ± 0.04
MgO					
MnO	4.94 ± 0.15	6.6 ± 0.25	7.89 ± 0.28	5.93 ± 0.24	5.67 ± 0.50
CaO	48.28 ± 0.24	46.93 ± 0.37	47.51 ± 0.35	47.34 ± 0.49	49.23 ± 0.46
K ₂ O	0.14 ± 0.03	0.19 ± 0.05	0.07 ± 0.03	0.13 ± 0.02	0.02 ± 0.00
Na ₂ O	0.59 ± 0.04	0.60 ± 0.05	0.06 ± 0.03	0.33 ± 0.04	0.13 ± 0.03
P ₂ O ₅	39.89 ± 0.46	39.81 ± 0.27	40.5 ± 0.47	39.7 ± 0.63	40.83 ± 0.49
Cl	6.03 ± 0.38	5.20 ± 0.60	0.94 ± 0.05	5.79 ± 0.91	1.15 ± 0.02
F					
Total	100.27 ± 0.64	99.87 ± 0.62	97.28 ± 0.51	99.72 ± 0.65	97.11 ± 0.39
H ₂ O	0.09		1.40	0.17	1.43
CO ₂	0.08		0.07	0.04	0.06
Al	0.01	0.01		0.01	
Fe					0.02
Mg					
Mn	0.74	0.99	1.16	0.89	0.83
Ca	9.12	8.86	8.84	8.99	9.12
K	0.06	0.09	0.03	0.06	0.01
Na	0.20	0.21	0.02	0.11	0.04
Sum Ca Site	10.13	10.15	10.06	10.06	10.03
P	5.95	5.94	5.96	5.95	5.98
Si	0.05	0.07	0.04	0.07	0.03
Sum P site	6.00	6.01	6.00	6.02	6.01
Cl	1.80	1.55	0.28	1.74	0.34
F					
H ₂ O	0.11		1.62	0.20	1.65
Sum X site	1.91		1.90	1.94	1.99
X ^{Ap} Cl	0.89		0.14	0.85	0.17
X ^{Ap} F					
X ^{Ap} H ₂ O	0.05		0.77	0.09	0.79
X ^{Ap} total	0.94		0.91	0.94	0.96
D _{Mn} ^{ap/m}	0.54	1.53	0.87	0.89	0.75
D _{H₂O} ^{ap/m}	0.10		0.18	0.06	0.18
K _D ^{Cl-H₂O}	21.18		0.22	5.30	0.21
K _{DF} ^{F-H₂O}					

20

21

22

23

24 Table 3 continued

	MW 1200 Hap10	Cr 1200 Hap10	NNO 1200 Hap10	Cr 1200 Hap5
# Analyses	4	8	7	6
SiO ₂	0.55 ± 0.23	0.23 ± 0.02	0.27 ± 0.02	0.27 ± 0.02
Al ₂ O ₃				
FeO ^T	0.67 ± 0.12			
MgO	0.15 ± 0.01	0.03 ± 0.00		0.06 ± 0.01
MnO	7.14 ± 0.49	7.30 ± 0.61	6.61 ± 0.06	6.58 ± 0.08
CaO	46.57 ± 0.66	47.76 ± 0.57	48.11 ± 0.21	48.24 ± 0.22
K ₂ O	0.11 ± 0.04	0.06 ± 0.02	0.05 ± 0.01	0.04 ± 0.01
Na ₂ O	0.28 ± 0.03	0.08 ± 0.02	0.19 ± 0.03	0.18 ± 0.07
P ₂ O ₅	40.24 ± 0.59	40.92 ± 0.56	40.51 ± 0.50	41.21 ± 0.29
Cl	1.89 ± 0.10	0.63 ± 0.04	1.93 ± 0.03	0.74 ± 0.05
F	0.24 ± 0.30			
Total	97.86 ± 0.60	96.73 ± 0.65	97.41 ± 0.64	97.15 ± 0.27
H ₂ O		1.63	1.35	1.54
CO ₂		0.08	0.11	0.08
Al				
Fe	0.10			
Mg	0.04	0.01		0.02
Mn	1.06	1.07	0.97	0.96
Ca	8.71	8.85	8.98	8.90
K	0.05	0.03	0.02	0.02
Na	0.09	0.03	0.06	0.06
Sum Ca Site	10.05	9.98	10.04	9.95
P	5.95	5.99	5.97	6.01
Si	0.08	0.03	0.04	0.04
Sum P site	6.03	6.02	6.01	6.04
Cl	0.56	0.18	0.57	0.22
F	0.13			
H ₂ O		1.88	1.57	1.77
Sum X site		2.07	2.14	1.98
X ^{Ap} Cl		0.09	0.28	0.11
X ^{Ap} F				
X ^{Ap} H ₂ O		0.90	0.75	0.85
X ^{Ap} total		0.99	1.03	0.96
D _{Mn} ^{ap/m}	1.00	1.02	0.86	1.70
D _{H₂O} ^{ap/m}		0.21	0.24	0.24
K _D ^{Cl-H₂O}		0.28	0.40	0.90
K _{DF} ^{F-H₂O}				

25

26

27

28

29

30

31 Table 3 continued

	SH3 Cr	SH3 PtC	SH3 Pt	SH3 MH
# Analyses	5	6	4	8
SiO ₂	0.39 ± 0.05	0.42 ± 0.06	0.39 ± 0.10	0.39 ± 0.10
Al ₂ O ₃				
FeO ^T				0.05 ± 0.04
MgO	0.88 ± 0.01	0.86 ± 0.02	0.90 ± 0.01	0.87 ± 0.02
MnO	0.16 ± 0.01	0.19 ± 0.01	0.18 ± 0.01	0.19 ± 0.02
CaO	54.3 ± 0.18	53.96 ± 0.23	54.51 ± 0.10	54.36 ± 0.45
K ₂ O		0.02 ± 0.01		0.02 ± 0.01
Na ₂ O				
P ₂ O ₅	41.28 ± 0.67	41.79 ± 0.48	41.39 ± 0.22	41.71 ± 0.39
Cl	0.02 ± 0.02	0.04 ± 0.01	0.03 ± 0.01	0.02 ± 0.02
F	3.24 ± 0.19	3.34 ± 0.12	3.61 ± 0.31	3.25 ± 0.18
Total	100.33 ± 0.58	100.71 ± 0.31	101.06 ± 0.19	100.92 ± 0.44
H ₂ O	0.37	0.26	0.20	0.40
CO ₂	0.28	0.21	0.43	0.24
Al				
Fe				0.01
Mg	0.22	0.22	0.23	0.22
Mn	0.02	0.03	0.03	0.03
Ca	9.85	9.74	9.86	9.79
K		0.01		0.01
Na				
Sum Ca Site	10.10	9.99	10.11	10.05
P	5.92	5.96	5.91	5.94
Si	0.05	0.06	0.05	0.05
Sum P site	5.97	6.02	5.97	5.99
Cl	0.01	0.01	0.01	0.01
F	1.74	1.78	1.93	1.73
H ₂ O	0.42	0.29	0.23	0.45
Sum X site	2.16	2.08	2.16	2.18
X ^{Ap} Cl		0.01		
X ^{Ap} F	0.86	0.89	0.96	0.86
X ^{Ap} H ₂ O	0.20	0.14	0.11	0.22
X ^{Ap} total	1.07	1.04	1.07	1.09
D _{Mn} ^{ap/m}	0.22	0.24	0.20	0.22
D _{H₂O} ^{ap/m}	0.23	0.30	0.11	0.21
K _D ^{Cl-H₂O}				
K _{DF} ^{F-H₂O}	4.38	3.21	9.90	4.43

32

33

34

35

36

37

38

	BMT2 Cr	BMT2 Pt	BMT2 MH
# Analyses	4	7	5
SiO₂	0.32 ± 0.11	0.17 ± 0.01	0.17 ± 0.02
Al₂O₃			
FeO^T		0.14 ± 0.02	0.61 ± 0.03
MgO	0.12 ± 0.01	0.10 ± 0.01	0.07 ± 0.00
MnO	0.15 ± 0.04	0.49 ± 0.06	0.27 ± 0.01
CaO	54.64 ± 0.45	54.44 ± 0.15	54.40 ± 0.23
K₂O	0.09 ± 0.04	0.06 ± 0.02	0.05 ± 0.01
Na₂O	0.11 ± 0.03	0.08 ± 0.02	0.09 ± 0.05
P₂O₅	41.47 ± 0.36	41.52 ± 0.52	41.82 ± 0.42
Cl			0.02 ± 0.02
F	3.53 ± 0.21	3.26 ± 0.13	3.40 ± 0.12
Total	100.5 ± 0.47	100.28 ± 0.50	100.94 ± 0.34
H₂O	0.16	0.26	0.36
CO₂	0.15	0.21	0.09
Al			
Fe		0.02	0.09
Mg	0.03	0.03	0.02
Mn	0.02	0.07	0.04
Ca	9.93	9.90	9.84
K	0.04	0.03	0.02
Na	0.04	0.03	0.03
Sum Ca Site	10.06	10.07	10.03
P	5.96	5.96	5.98
Si	0.05	0.02	0.02
Sum P site	6.00	5.99	6.00
Cl			0.01
F	1.89	1.75	1.82
H₂O	0.18	0.29	0.41
Sum X site	2.07	2.04	2.23
X^{Ap}Cl			
X^{Ap}F	0.94	0.87	0.90
X^{Ap}H₂O	0.09	0.14	0.20
X^{Ap}total	1.03	1.01	1.10
D_{Mn}^{ap/m}	2.14	0.65	0.47
D_{H₂O}^{ap/m}	0.34	0.16	0.19
K_D^{Cl-H₂O}			
K_{DF}^{F-H₂O}	6.50	14.39	7.94

39

Table 4: Major element compositions of Mn granitic and Fe-Mn granitic glasses synthesised in a 1 atm. Gas mixing furnace under reducing conditions. Errors represent 1σ .

A - Mn granitic glasses							
Log fO₂	-0.7	<-4	-5.1	-6.3	-7.8	-8.9	-9.4
SiO₂	61.20 ± 1.22	62.40 ± 1.04	61.66 ± 0.54	62.01 ± 0.73	60.76 ± 1.27	62.85 ± 1.70	63.48 ± 0.55
Al₂O₃	19.06 ± 0.39	17.64 ± 0.52	17.89 ± 0.66	18.07 ± 0.29	18.61 ± 0.70	17.62 ± 0.91	17.93 ± 0.10
FeO^T							
MnO	8.64 ± 0.75	8.70 ± 0.58	9.26 ± 0.35	9.25 ± 0.34	9.23 ± 0.42	9.29 ± 0.93	6.55 ± 0.80
K₂O	6.68 ± 0.18	6.80 ± 0.18	6.81 ± 0.07	6.82 ± 0.14	6.59 ± 0.15	6.39 ± 0.12	7.10 ± 1.25
Na₂O	4.83 ± 0.08	4.73 ± 0.17	4.75 ± 0.10	4.64 ± 0.07	4.58 ± 0.09	4.14 ± 0.12	4.38 ± 0.74
Total	100.54 ± 0.69	100.37 ± 0.45	100.48 ± 1.12	100.90 ± 0.32	99.88 ± 0.61	100.41 ± 0.53	99.56 ± 0.80

B - Mn-Fe granitic glasses							
Log fO₂	-0.7	<-4	-5.1	-6.3	-7.8	-8.9	-9.4
SiO₂	59.67 ± 1.37	60.62 ± 1.19	57.00 ± 0.75	61.28 ± 1.34	60.41 ± 2.26	61.33 ± 0.86	61.10 ± 2.03
Al₂O₃	19.36 ± 0.90	18.08 ± 0.97	18.43 ± 0.13	18.56 ± 0.66	17.78 ± 0.60	16.95 ± 0.26	17.75 ± 0.52
FeO^T	4.81 ± 0.17	5.40 ± 0.11	7.61 ± 0.17	8.43 ± 0.66	6.65 ± 0.97	7.05 ± 0.25	6.06 ± 0.89
MnO	3.91 ± 0.36	3.58 ± 0.27	4.38 ± 0.11	4.13 ± 0.35	3.75 ± 0.58	3.64 ± 0.12	3.48 ± 0.53
K₂O	6.96 ± 0.19	7.02 ± 0.08	6.78 ± 0.07	3.88 ± 0.22	6.71 ± 0.23	6.76 ± 0.11	7.01 ± 0.21
Na₂O	5.02 ± 0.11	4.88 ± 0.13	4.83 ± 0.20	3.16 ± 0.12	4.57 ± 0.10	4.38 ± 0.16	4.39 ± 0.12
Total	99.76 ± 0.41	99.60 ± 0.52	99.07 ± 0.51	99.48 ± 0.24	99.90 ± 0.50	100.14 ± 0.55	99.80 ± 0.41

40

41

42 **Table 5:** Pre edge peak fitting for PM1 Pt, PM1 PtC and PM1 NNO. Apt = apatite.

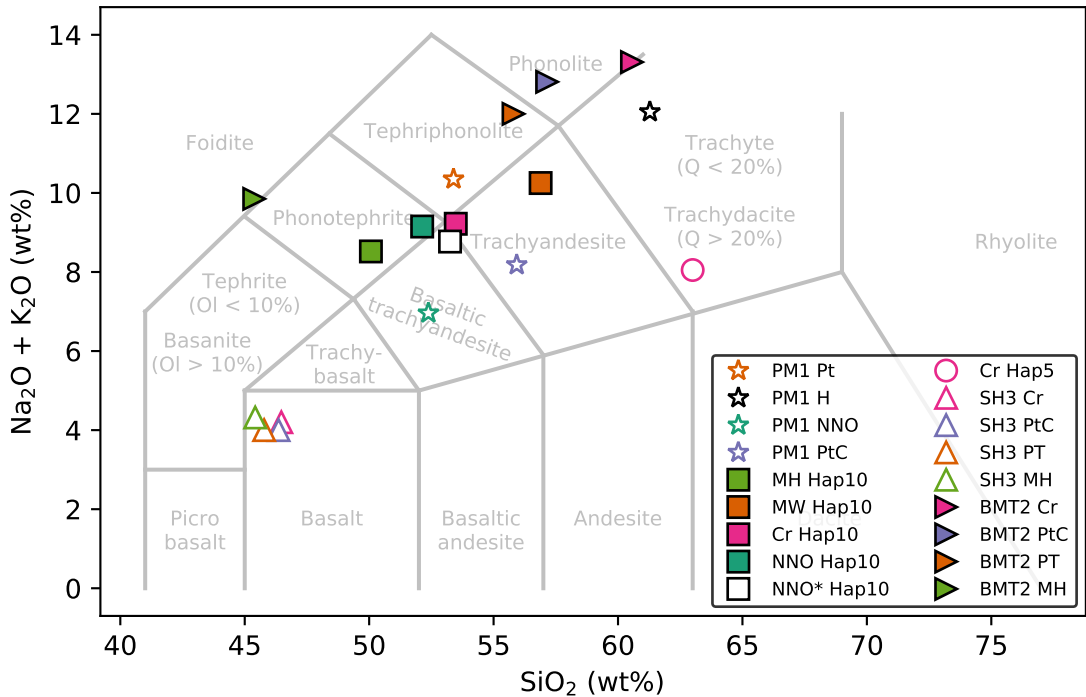
43

Sample	Centroid (eV)	Intensity
PM1 Pt Glass	6540.46	0.078
PM1 PtC Glass	6540.43	0.080
PM1 NNO Glass	6540.46	0.071
PM1 Pt Apt.	6540.44	0.064
PM1 PtC Apt.	6540.44	0.063
PM1 NNO Apt.	6540.49	0.054

44

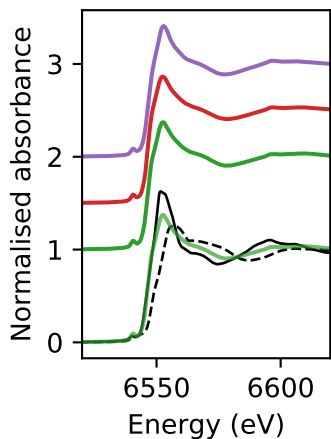
Table 6: Whole rock geochemistry for thought to be representative of the four petrologic zones at the Criffel Pluton. ¹Values from (Miles et al., 2013). ²Values from (Stephens & Halliday, 1980).

	Zone 1 (09-17) ¹	Zone 2 (09-18) ¹	Zone 3 (09-21) ¹	Zone 4 (274) ²
SiO ₂	63.92	66.04	69.52	71.35
TiO ₂	0.58	0.53	0.36	0.21
Al ₂ O ₃	15.75	15.33	15.10	15.39
FeO ^T	3.24	2.74	1.89	1.33
MnO	0.06	0.05	0.04	0.04
MgO	2.51	1.97	0.93	0.97
CaO	3.82	2.67	2.02	0.90
K ₂ O	3.35	3.86	4.20	4.70
Na ₂ O	4.12	3.99	3.84	3.84
P ₂ O ₅	0.29	0.26	0.17	0.10
NBO/T	0.18	0.13	0.06	0.03

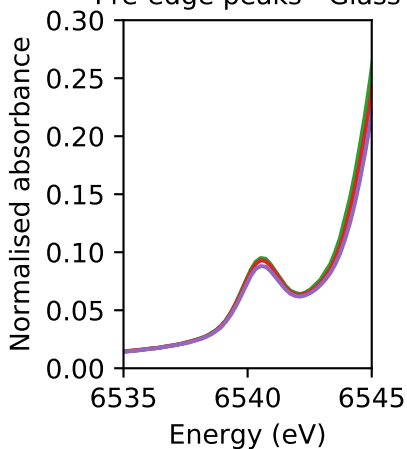


A

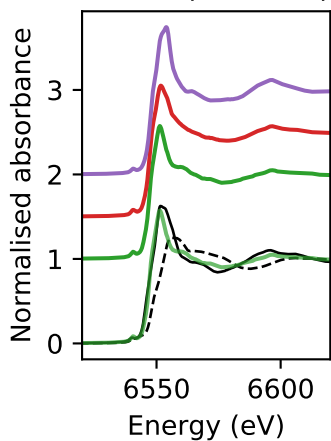
Normalised spectra - Glass

**B**

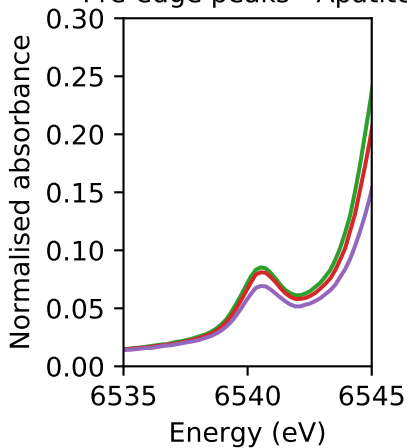
Pre-edge peaks - Glass

**C**

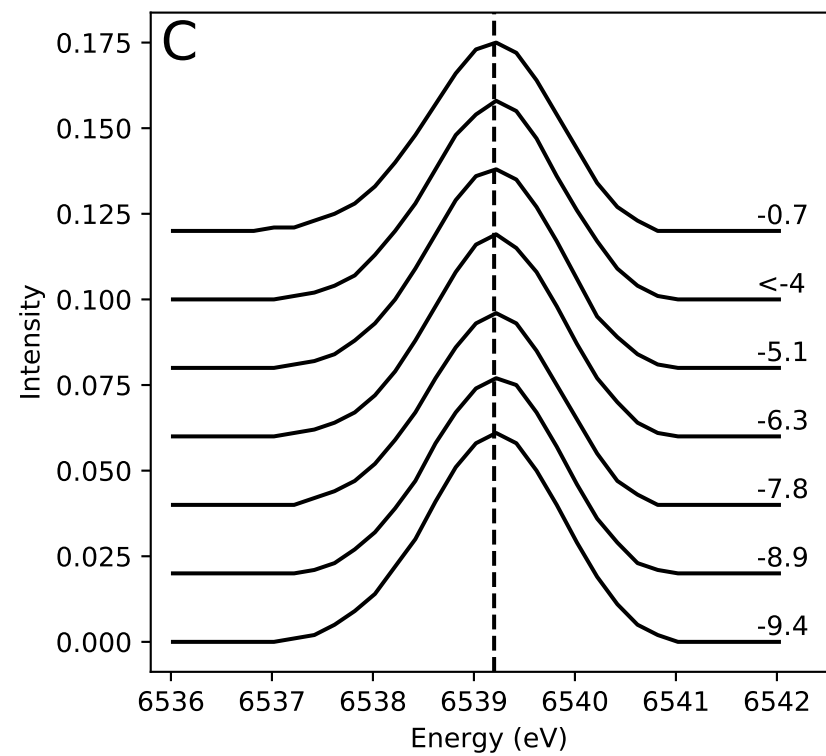
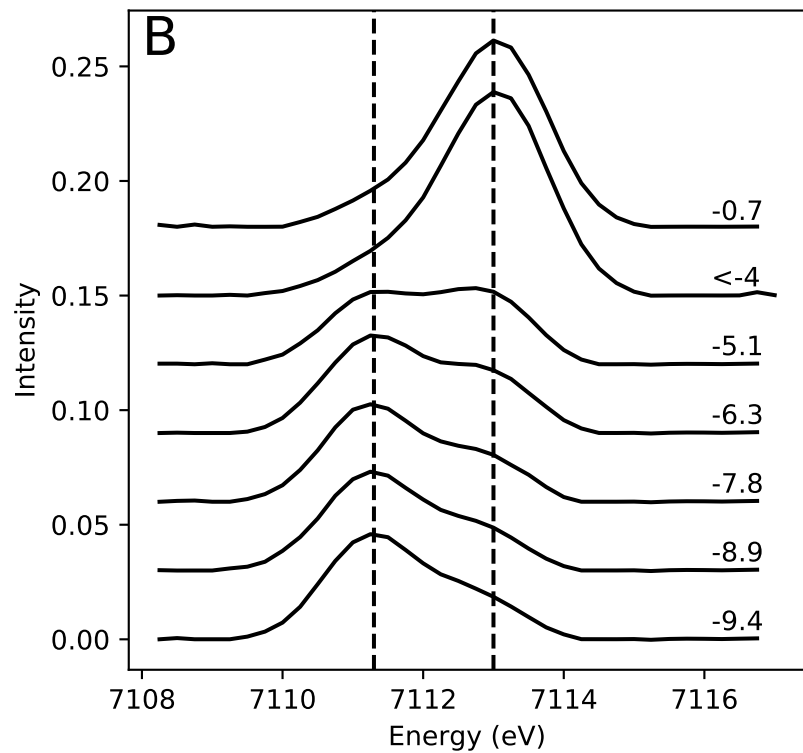
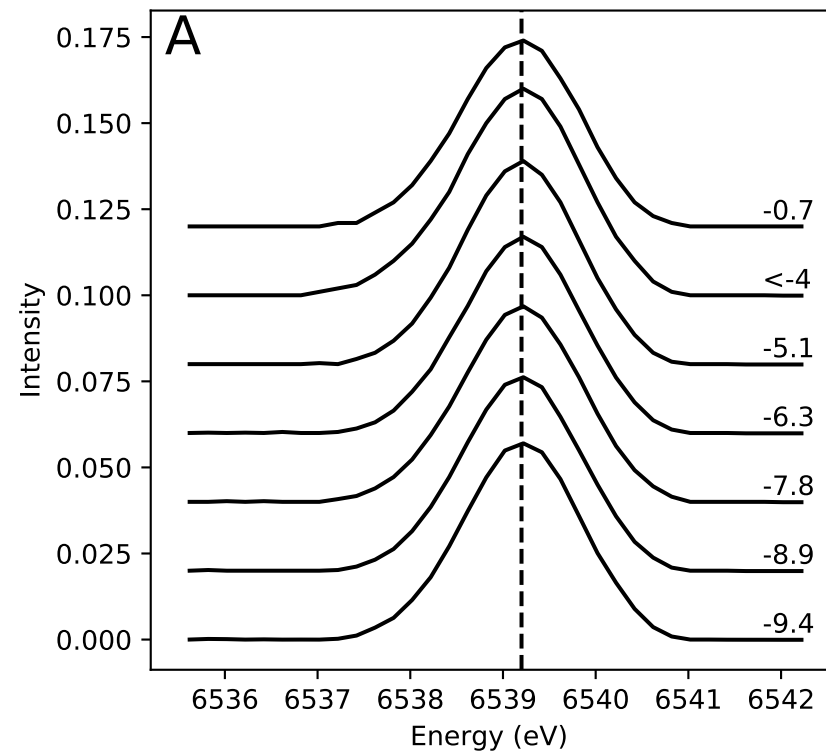
Normalised spectra - Apatite

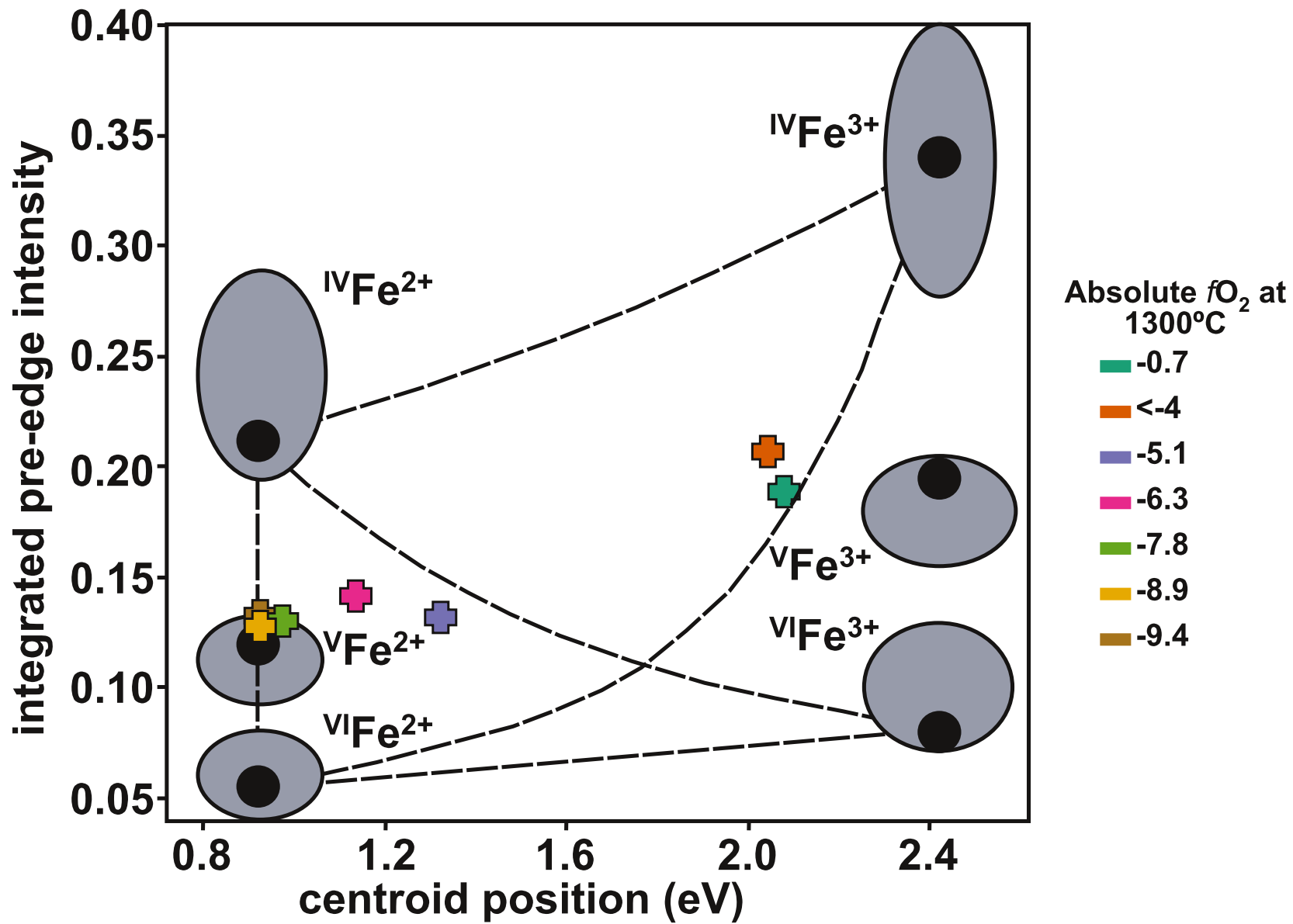
**D**

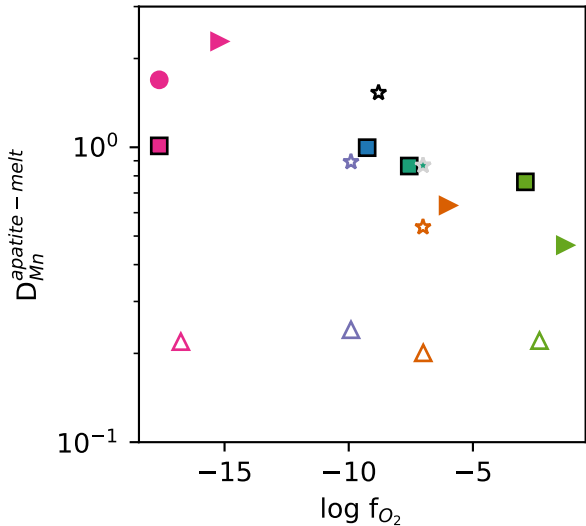
Pre-edge peaks - Apatite



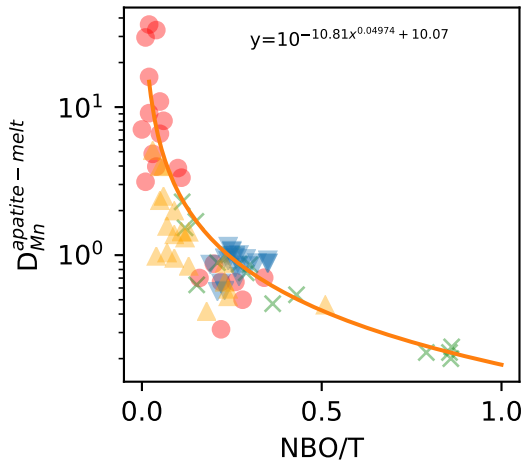
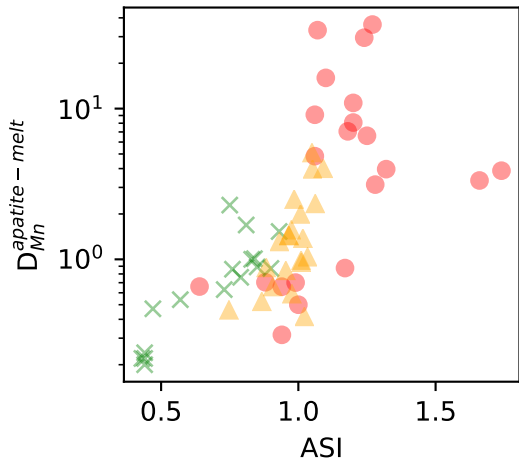
---- Mn_2O_3 — Tephroite — Pt — PtC — NNO







- | | | | |
|---|-----------|---|---------|
| ☆ | PM1 Pt | ● | Hap5 Cr |
| ★ | PM1 H | △ | SH3 Cr |
| ☆ | PM1 NNO | △ | SH3 PtC |
| ☆ | PM1 PtC | △ | SH3 Pt |
| ■ | Hap10 MH | △ | SH3 MH |
| ■ | Hap10 MW | △ | BMT2 Cr |
| ■ | Hap10 Cr | △ | BMT2 Pt |
| ■ | Hap10 NNO | △ | BMT2 MH |

A**B**

● Sha and Chappell 1999
 × This study

▼ McCubbin et al. 2015
 ▲ Belousova et al. 2001

